Two-fluid solutions for Langmuir probes in collisionless and isothermal plasma, over all space and bias potential

Ph. Guittienne,[1] A. A. Howling,[2] and I. Furno[2]

[1] *Helyssen, Route de la Louche 31, CH-1092 Belmont-sur-Lausanne, Switzerland*

[2] *Ecole Polytechnique Fédérale de Lausanne (EPFL), Swiss Plasma Center, CH-1015 Lausanne, Switzerland*

This paper presents solutions for the classical one-dimensional (radial and Cartesian) problem of Langmuir probes in a collisionless, isothermal plasma. The method is based on two-fluid equations derived from the first two moments of Vlasov's equation. In contrast to commonly-used approximations, electron inertia and ion temperature are not neglected so that the fluid equations are symmetric in the terms for electrons and ions. The fluid equations are reduced analytically so that the electric potential is the only remaining spatial function, which is numerically determined using Poisson's equation. The single radial solution applies continuously over the whole region from the probe up to the unperturbed plasma, in contrast to theories which separate the probe boundary region into a charged sheath and a quasi-neutral pre-sheath, and is valid for all values of probe bias potential. Current-voltage characteristics are computed for cylindrical and spherical probes, which exhibit non-saturation of the ion and electron currents. The 1D Cartesian case is also analysed, and the Bohm criterion is recovered only in the limit of large radius probes.

I. INTRODUCTION

A body immersed in a plasma acts as a sink for charged particles. Because of the large difference in mobility between electrons and ions, the former tend to be lost more rapidly to the body, thus creating a charged region in the vicinity of the surface, commonly called the sheath. When the immersed object is electrically floating, the space charge distribution in the sheath evolves towards an equilibrium where ion and electron fluxes are equal and no more charge is transferred to the body. If the immersed object is biased, the sheath adapts to the imposed boundary potential and a current is collected.

A fundamental diagnostic in plasma physics, the Langmuir probe, relies on the analysis of the current-voltage characteristic obtained by sweeping the bias potential on an immersed metallic pin. The method is technically simple, but the analysis of Langmuir probe characteristics is difficult, mainly because of the theoretical issues inherent to the plasma sheath problem.[1] This was notably addressed by Langmuir and colleagues[2,3] and has since been a major topic in plasma physics. A fundamental set of equations involved in this problem arises from the moments of Boltzmann's equation which describe the electrons and ions as two fluids in terms of their mean densities and velocities. The successive moments by themselves do not constitute a closed set of equations and have to be completed by a closure expression. Furthermore, the two fluid equations are coupled through Poisson's equation which determines the electric potential.

In the early stages of sheath theory,[4] Langmuir introduced two approximations which have been almost universally adopted up till now: The first is to separate the continuous region next to the probe into a space-charge sheath and a quasi-neutral plasma;[1–18] the interpretation of the plasma-sheath transition has caused much debate.[1,4,15,16] The second approximation is to neglect the electron inertia in the associated momentum conservation equation, which results in the commonly-used Boltzmann relation for the electron density,[1–28] $n_e = n_0 \exp \frac{\Delta V}{T_e}$, where ΔV and T_e are respectively a potential difference and the electron temperature, here expressed in volts.[28]

In this work, we present two-fluid solutions of a collisionless, isothermal plasma with singly-charged positive ions, for the simplified situations of one-dimensional (1D) radial and Cartesian geometries. To be precise, the problem is solved analytically until the point where Poisson's equation has to be integrated, which is performed numerically. Specific features of the solution method are the retainment of electron inertia and ion temperature in the fluid momentum equations, the use of Lambert's function,[29–31] and the respect of particle flux conservation everywhere from the unperturbed plasma up to the probe surface. Boundary conditions are of prime importance because they define the probe fluxes; these are calculated from the self-consistent convective flow velocity of each species.

As a first consequence, the separation of space into sheath and quasi-neutral plasma regions is no longer necessary for radial probes because a single, collisionless solution is considered. Secondly, the fluid equations are symmetric in the terms for electrons and ions (accounting for charge sign), hence the solution is valid for all probe bias voltages. Current-voltage characteristics can be derived analytically for the 1D Cartesian case, whereas for cylindrical and spherical probes, two parameters still have to be determined numerically.

A. Brief review of probe theory

The dominant approach to describe the perturbed region adjacent to a plane probe consists in splitting this region into two distinct ones. The first sub-region, the sheath, extends from the probe surface to a point, the sheath entrance, at which the electron and ion densities are taken to be equal. Beyond this point there extends a second sub-region, the pre-sheath, characterized by the quasi-neutrality hypothesis. Collisionless and isothermal 1D Cartesian models are generally applied to describe the sheath region, which is then characterized by constant particle fluxes. The Bohm criterion[5] was developed to account for the ion velocity at the sheath entrance. Ionization must then be considered to provide the necessary ion flux in the pre-sheath. This division between sheath and pre-sheath regions gives rise to 2-scale theories.[3,5,6,11,12] Different assumptions and approximations are made in these domains, for example, collisional ionisation in the pre-sheath and no collisions in the sheath,[6] so it is clear that matching problems will occur at the sheath/pre-sheath interface.[7,12] This can be partly redressed by interposing another domain, a transition layer, on an intermediate scale, which accounts for space charge and the dominant pre-sheath processes.[12] In this way, as more layers are added, the approximations are successively improved for the various scale lengths. It is clear, however, that a single analytical solution for plasma-to-wall is precluded, by definition.[7] Ideally, the exact Boltzmann equation would be solved over the whole region to give a single solution. In the absence of such analytical solutions, single profiles were obtained by numerical computations which do not require multi-scale assumptions[7,32–35] although their accuracy of course depends on any approximations made. Furthermore, real finite-sized plane probes collect ions from an ill-defined hemispherical shape so that, in practice, an infinite plane wall plasma-sheath transition does not exist[1,20] and at least a 2D approach would be necessary.[31]

To avoid the difficulties associated with infinite plane walls, this paper goes on to consider a two-fluid, 1D solution for radial Langmuir probes (cylindrical and spherical) in collisionless, isothermal plasma. The term "fluid" conventionally refers to collisional conditions; however, the macroscopic variables for electrons and ions are here described by velocity moments of two collisionless distribution functions, often known as a two-fluid approach. In the case of radial probes, the ion acceleration due to inward flux concentration in the "geometric pre-sheath" means that a collisionless pre-sheath solution relaxes asymptotically to the unperturbed, field-free plasma at infinity, without requiring ionisation or other collisional processes which are necessary in the 1D plane wall situation.[11,12] Hence a collisionless, single, 1D radial solution would appear possible for both the sheath and the pre-sheath, i.e. over the whole domain.[1] In fact, the applicability,[18] or necessity,[1,7,20,35] of the Bohm criterion is less clear for cylindrical and spherical probe geometries. Calculations in the limit of probe radius much larger than the sheath width[36] are used here to reconcile the 1D radial model with conventional 1D sheath/pre-sheath models[11,12] which invoke the Bohm criterion.

Fluid models for non-saturated probe ion currents calculate the increase of the effective ion collection area due to a thicker sheath at higher values of probe bias voltage. Non-saturated currents are also predicted in the framework of kinetic approaches, notably in orbital-motion-limited (OML) theories.[2,8,19,21,27] In these, the conservation of individual particle angular momentum plays a central role. In the present work, we develop a two-fluid solution under the hypothesis of isotropic temperatures and Maxwellian distributions. These assumptions are common,[11,25,30–32] and fair agreement is found with a kinetic model.[37] However, it means that any distortions of the Maxwellian distributions due to truncation,[7,27,31,38,39] anisotropic temperatures,[37] angular momentum conservation or trapped orbits[21,32] cannot be accounted for. This does not mean that kinetic effects are unimportant; in fact, orbital motion kinetic effects are expected to be more and more relevant as the probe diameter becomes smaller, making the assumption of Maxwellian distributions close to the probe surface less valid. This is probably a limit of validity of the present Maxwellian approach. To have a better two-fluid collisionless description, one should calculate the distortions of the distribution functions due to kinetic effects (such as in OML theory) before performing Vlasov equation moments. Instead, this two-fluid model tacitly assumes that like-particle collisions are sufficiently frequent to maintain Maxwellian distributions, even near to an adsorbing wall, but that unlike-particle collisions are sufficiently rare for friction and ionisation to be negligible. Alternatively, there may be other processes, such as turbulence or electric field micro-instabilities, which maintain a Maxwellian distribution even when collisions are rare; this is known as Langmuir's paradox.[25] Finally, fluctuations and instabilities such as ion acoustic waves could affect experimental measurements but are not considered in the stationary solutions presented here.[31,40] To summarize, this fluid model might not represent physical situations generally, but it is a solution to a classical problem of probes in collisionless, isothermal plasma.

B. Structure of the paper

The analytical model for a probe in a collisionless plasma is developed in three stages corresponding to the three geometries in Fig. 1:

1. Fig. 1(a) shows a 1D Cartesian model for collisionless plasma flow to an infinite plane wall. The wall does not represent a non-intrusive Langmuir probe causing only a small perturbation to the plasma.[1,31] Nevertheless, this 1D Cartesian model serves the purpose of introducing the mathematical method in
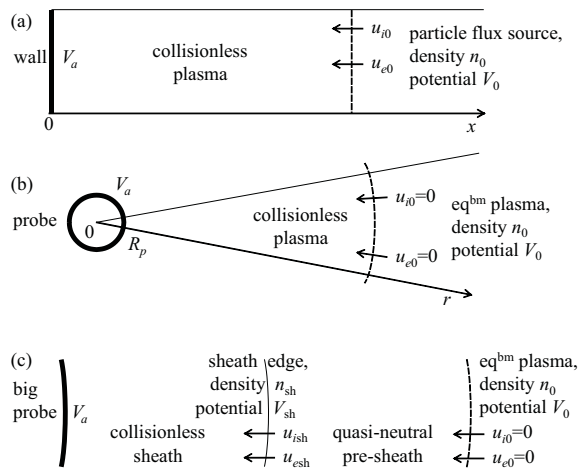
FIG. 1. Basic description of the probe geometries, showing the probe applied voltage V_a, and the ion and electron convective velocities u_{i0} and u_{e0}. The dashed lines represent the limit of large distance from the probe up to the equilibrium plasma at infinity. (a) Infinite plane wall (1D Cartesian solution) in Section II, with incoming particle velocities from a supposed plasma source at infinity.[41] (b) Cylindrical and spherical probes (1D radial solution) of Sections III and IV, with vanishing particle velocity from infinity. (c) Big radius probe in Section V, with space charge sheath and quasi-neutral pre-sheath, showing the ion and electron convective velocities u_{ish} and u_{esh} at the plasma-sheath interface.

Section II, and provides a comparison in the limit of large-radius probes in Section V.

2. Fig. 1(b) shows a 1D radial model to represent collisionless plasma flow to a probe. In contrast to the 1D Cartesian model, the flux to a small radius Langmuir probe causes only a small perturbation to the plasma, which is maintained by some independent source. Almost all of the ionisation rate due to this independent source is assumed to be in equilibrium with particle loss rates to other electrodes and surfaces. The assumption of collisionless plasma in the locality of the probe remains a reasonable approximation for a perturbed region around the probe which is small compared to the mean free path for particle collisions. The length-scale of the solution then determines the lower limit of the mean free path and hence the upper pressure limit for solution validity.[34] For perturbation scale lengths < 1 mm calculated in this work, collisionless conditions are expected to be satisfied for argon gas pressures up to about 1 Pa, where the mean free path for collisions $\lambda_c \sim 1$ cm (for ion charge-exchange collision cross-sections[28,34] $\sim 4 \cdot 10^{-19}$ m^2). Cylindrical and spherical probe 1D radial solutions are presented in Sections III and IV respectively.

3. Fig. 1(c) shows part of the wall of a big radius probe in a 1D radial model. Section V compares the limit

of large probe radius with the 1D Cartesian plane wall solution and a classical sheath model.

Discussions and conclusions are presented in Sections VI and VII respectively. Finally, Appendixes A and B explain the Lambert solution and describe a practical method to interpret probe IV characteristics.

II. 1D CARTESIAN CASE OF AN INFINITE PLANE WALL

A. Conservation of particles and of momentum for electrons and ions

Taking the first velocity moment of Vlasov's equation, a momentum conservation equation for ions and electrons can be written for a two-fluid description as follows:

$$m_s n_s \left[\frac{\partial \mathbf{u}_s}{\partial t} + (\mathbf{u}_s.\nabla)\mathbf{u}_s \right] = q_s n_s \mathbf{E} - \nabla \cdot \mathbf{P}_s, \quad (1)$$

for a collisionless, non-magnetized plasma, where n_s is the number density of species s, $\mathbf{u}_s$ the convective velocity, m_s the particle mass, q_s the electric charge (sign included), $\mathbf{P}_s$ the pressure tensor, and $\mathbf{E}$ the electric field.

We consider here the 1D Cartesian problem ($\nabla \rightarrow \partial_x$) of a semi-infinite plasma facing a wall with steady state flow ($\partial_t \rightarrow 0$) in Fig. 1(a). The solutions here are restricted to the case of electrons and a single ion species with a single positive charge ($|q_s| = q$, the elementary charge). The treatment of different ion species, multiply-charged ions, and negative ions, although possible, is beyond the scope of this work. As a closure expression for (1) we assume an isothermal relation for equilibrium, with isotropic Maxwellian velocity distributions for each species.[25,31,40] Under these conditions the pressure tensor is diagonal and isotropic, and by using the ideal gas law the scalar pressure can be expressed as $p_s = n_s q T_s$. Here, T_s is the s species mean temperature defined in volts in order to simplify expressions involving ratios of voltage and temperature.[28] The relation between T_s in volts, and the temperature T_s in Kelvin, is given by $q T_s = k_\mathrm{B} \mathrm{T}_s$, where k_B is Boltzmann's constant, by which the conventional expressions can be recognised.

The resulting fluid equations for electron and ion momentum are:

$$m_e n_e u_e \partial_x u_e - q n_e \partial_x V + q T_e \partial_x n_e = 0,$$
$$m_i n_i u_i \partial_x u_i + q n_i \partial_x V + q T_i \partial_x n_i = 0, \quad (2)$$

where V is the electric potential. Here, the densities, fluid velocities, and potential are all functions of x.

In the literature, at this point, the electron inertia convective term (proportional to m_e) is almost universally neglected in (2), and as such, the electron density is described by a Boltzmann relation.[1–28] Furthermore, the cold ion approximation is usually applied ($T_i = 0$) in which case the ion pressure gradient is neglected and (2)

leads to the free fall solution for the ion density. A consequence of these approximations is that the sheaths are only properly described for large negative bias potentials with respect to the plasma potential. In the following, we break with tradition and keep all terms in (2). In fact, the only way to guarantee validity for the whole range of probe bias potential is to maintain symmetry between the electron and ion terms.[32] It will be seen that the electron and ion variables are interchangeable in all the exact expressions - accounting for charge sign - as is necessary for a model where the probe bias potential can be lower or higher than the plasma potential.

We assume $n_e, n_i \neq 0$ for all x, and define thermal velocities $u_{\mathrm{the}} = \sqrt{qT_e/m_e}$ and $u_{\mathrm{thi}} = \sqrt{qT_i/m_i}$, the root mean square velocity in any single direction. The mathematical expressions can be simplified by introducing the dimensionless functions U_e, U_i which are the squares of the convective velocity normalized to the thermal velocity, for electrons and ions respectively:

$$U_e = \left(\frac{u_e}{u_{\mathrm{the}}}\right)^2 \quad \text{and} \quad U_i = \left(\frac{u_i}{u_{\mathrm{thi}}}\right)^2.$$

Equations (2) then become:

$$\frac{1}{2}\partial_x U_e - \frac{1}{T_e}\partial_x V + \partial_x \ln(n_e) = 0,$$
$$\frac{1}{2}\partial_x U_i + \frac{1}{T_i}\partial_x V + \partial_x \ln(n_i) = 0. \tag{3}$$

Neglecting ionisation and recombination processes, consistent with the collisionless assumption, the particle flux conservation is expressed from the zeroth moment of Vlasov's equation as:

$$\partial_t n_s + \nabla \cdot (n_s \mathbf{u}_s) = 0, \tag{4}$$

which, according to our assumptions, leads to:

$$\partial_x(n_e u_e) = 0, \quad \text{and} \quad \partial_x(n_i u_i) = 0. \tag{5}$$

Equations (3) and (5) can be directly integrated to give:

$$\frac{U_e}{2} - \frac{V}{T_e} + \ln(n_e) = C_e,$$
$$\frac{U_i}{2} + \frac{V}{T_i} + \ln(n_i) = C_i, \tag{6}$$
$$n_e u_e = \phi_e, \quad \text{and} \quad n_i u_i = \phi_i, \tag{7}$$

where the integration constants C_e, C_i, ϕ_e, ϕ_i depend on the boundary conditions. ϕ_e, ϕ_i are the constant flux densities (particles per second per unit area) for electrons and ions respectively. Electrons and ions are assumed to disappear by neutralization at the wall, with no processes such as secondary emission. For the plasma at infinity, we set an equal density n_0 for electrons and ions, and the plasma potential is set to V_0. Because we aim to treat the artificial 1D Cartesian problem of a semi-infinite collisionless plasma facing a plane wall, we must, considering (7), set non-vanishing injection velocities u_{s0} from infinity to ensure the conservation of particle fluxes, as shown
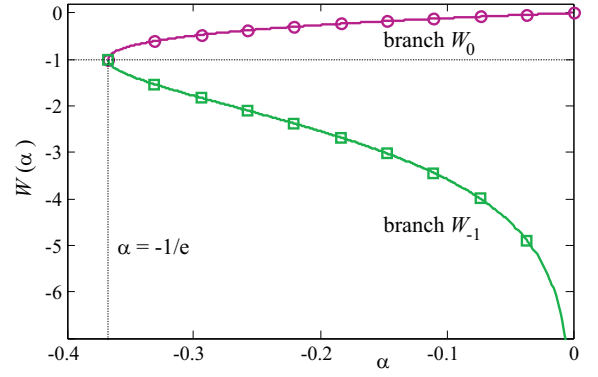

FIG. 2. Plot of the Lambert function branches W_0 (circles) and W_{-1} (squares) which have purely real and negative values for $-\frac{1}{e} \leq \alpha \leq 0$.

in Fig. 1(a). We therefore define the non-vanishing values at infinity for the normalized square velocities to be $U_{s0} = (u_{s0}/u_{\mathrm{ths}})^2$. Applying these boundary conditions to (6) and (7), the integration constants C_e, C_i, ϕ_e and ϕ_i are determined so that we can express n_e and n_i as:

$$n_e = n_0 \exp\left(\frac{U_{e0} - U_e}{2} + \frac{V - V_0}{T_e}\right),$$
$$n_i = n_0 \exp\left(\frac{U_{i0} - U_i}{2} - \frac{V - V_0}{T_i}\right), \tag{8}$$

and the particle flux conservation (7) as:

$$n_e^2 U_e = n_0^2 U_{e0}, \quad \text{and} \quad n_i^2 U_i = n_0^2 U_{i0}.$$

The particle density equations (8) are a more general form of the Boltzmann relation, known as the "Boltzmann distribution law" in kinetic theory, where the density, fluid velocity and potential can be non-uniform.[42] Combining these relations to eliminate the particle densities gives expressions for the particle fluid velocities in terms of the potential:

$$-U_e e^{-U_e} = -U_{e0} e^{-U_{e0} - \frac{2(V - V_0)}{T_e}},$$
$$-U_i e^{-U_i} = -U_{i0} e^{-U_{i0} + \frac{2(V - V_0)}{T_i}}. \tag{9}$$

The transcendental equations (9) have for solutions:

$$U_e = -W\left[-U_{e0} e^{-U_{e0} - \frac{2(V - V_0)}{T_e}}\right] = -W[\alpha_e],$$
$$U_i = -W\left[-U_{i0} e^{-U_{i0} + \frac{2(V - V_0)}{T_i}}\right] = -W[\alpha_i], \tag{10}$$

where W denotes the Lambert function[29] defined by $\alpha = z e^z \Leftrightarrow z = W[\alpha]$. This gives the functional dependence of the fluid velocities and densities on the electric potential, which is then the only remaining function to be determined using Poisson's equation. In the following we will first analyse the consequences of solutions (10); the full solution requiring integration of Poisson's equation is carried out in Sec. II D.

The Lambert function, which cannot be expressed in terms of elementary functions, is multi-valued and therefore has several branches. Because U_e and U_i are square velocities, the solutions (10) must be real and positive, which implies that the Lambert functions must be real and negative. Fortunately, regarding the former condition, only two branches of the Lambert function, W_0 and W_{-1}, have purely real values. Furthermore, in order to obtain negative values, the arguments for W_0 and W_{-1} must be restricted to the interval $[-\frac{1}{e}, 0]$. The representations of branches $W_0(\alpha)$ and $W_{-1}(\alpha)$ in this interval are shown in Fig. 2. The branch point, $\alpha = -\frac{1}{e}$, is of particular interest as it is the only value for which the condition $W_0(\alpha) = W_{-1}(\alpha)$ can be fulfilled. Note that, as $W_{0,-1}(-\frac{1}{e}) = -1$, the condition $\alpha_s = -\frac{1}{e}$ is equivalent to $u_s = u_{\text{th}s}$. Then, considering a given s species, the W_0 branch of the Lambert function must be applied to describe the fluid velocity u_s when it is known to be less than, or equal to, the thermal velocity. On the contrary, if $u_s \geq u_{\text{th}s}$, the fluid velocity must be described by the W_{-1} branch. Using these properties of the Lambert function, and under the important hypothesis of a monotonic spatial variation of the electric potential $V(x)$, from infinity where $V(x) = V_0$ up to the wall surface where a bias potential V_a is applied, the analysis of conditions $\alpha_{e,i} \in [-\frac{1}{e}, 0]$ (see Appendix A) leads to the following conclusions:

The applied potential $V_a = V_0$ plays a particular role in this problem because it corresponds to a field free situation. For $V_a < V_0$, ions are the attracted species and electrons are repelled, while the opposite happens when $V_a > V_0$. The roles of ions and electrons are then, in a way, symmetric with regard to the plasma potential.

For $V_a \leq V_0$:

$$U_e = -W_0 [\alpha_e] \quad \text{and} \quad U_i = -W_{-1} [\alpha_i], \quad (11)$$

with the conditions on initial velocities:

$$U_{i0} \geq 1,$$
$$0 \leq U_{e0} \leq U_{e0}^{\max} = -W_0 \left[-e^{\frac{2(V_a - V_0)}{T_e} - 1} \right] \leq 1. \quad (12)$$

The relations (12) imply that ions come from infinity with an initial convective velocity u_{i0} greater or equal to $u_{\text{th}i}$. The initial velocity of electrons, u_{e0}, is limited to a maximum value $u_{e0}^{\max}$. For $u_{e0} = u_{e0}^{\max}$, the electron velocity at the wall is also maximum and is equal to the thermal velocity $u_{\text{th}e}$.

For $V_a \geq V_0$:

$$U_e = -W_{-1} [\alpha_e] \quad \text{and} \quad U_i = -W_0 [\alpha_i], \quad (13)$$

with the conditions on initial velocities:

$$U_{e0} \geq 1,$$
$$0 \leq U_{i0} \leq U_{i0}^{\max} = -W_0 \left[-e^{-\frac{2(V_a - V_0)}{T_i} - 1} \right] \leq 1. \quad (14)$$

As stated above, the roles of electrons and ions are inverted when V_a crosses the plasma potential value, so that electrons now come from infinity with an initial convective velocity higher than their thermal velocity, while the maximal ion velocity at the wall is $u_{\text{th}i}$.

Now consider the $V_a = V_0$ case. Obviously, the solutions for $V_a \leq V_0$ (11) and $V_a \geq V_0$ (13) must give the same value for $V_a = V_0$. This leads to the condition $W_0(\alpha_{e,i}) = W_{-1}(\alpha_{e,i})$, which was shown to be satisfied only for $\alpha_{e,i} = -\frac{1}{e}$, and is equivalent to $U_i = U_e = 1$. Then, the convective velocity for both species must be $u_{\text{th}s}$ from infinity up to the wall. This notably implies that the flux density at the wall in the field-free situation is given by $\phi_s = n_0 u_{\text{th}s} = n_0 \sqrt{\frac{qT_s}{m_s}}$. This is different from the classical kinetic theory flux density $\phi_s = \frac{1}{4} n_0 \bar{v}_s = \frac{1}{\sqrt{2\pi}} n_0 u_{\text{th}s}$, (where $\bar{v}_s = \sqrt{\frac{8qT_s}{\pi m_s}}$ is the mean thermal velocity) which is conventionally assumed for the repelled species at the wall surface in sheath models.[1–3,8,9,13,19,26–28,32,43,44] We will come back to this point in the final discussion, Section VI B.

B. Criterion on initial velocities

To complete the solutions we have to determine U_{e0} and U_{i0}. A criterion on these initial velocities can be found, for any probe potential V_a, by requiring a monotonic decrease of the charge density modulus $|Q| = q|n_i - n_e|$ towards infinity where $V = V_0$; a local condition which can be expressed as $[\partial_V |Q|]_{V_0} \leq 0$.[45] According to our solution (10), after some algebra this inequality becomes:

$$T_i(U_{i0} - 1) + T_e(U_{e0} - 1) \geq 0. \quad (15)$$

This relation for the initial convective velocities, which is symmetric in electron and ion terms, can be seen as a generalization of the classical Bohm criterion.[5,11] By rewriting (15) in a more conventional way to express the minimal velocity for ions entering a sheath we obtain:

$$u_{i0} \geq \sqrt{\frac{q(T_e + T_i) - m_e u_{e0}^2}{m_i}}. \quad (16)$$

The Bohm criterion[5] $u_{i0} \geq u_{\text{Bohm}} = \sqrt{\frac{qT_e}{m_i}}$ is recovered for cold ions ($T_i = 0$) and negligible electron inertia ($m_e = 0$). Persson's[23] expression is obtained when ion temperature is accounted for, and the complete expression (16) of Baalrud et al[46] is recovered when electron inertia is also included. Note that criterion (15) implies a general coupling between ion and electron initial velocities for all bias potentials.

Interestingly, the inequality (15) is directly related to the required convective kinetic energy density at infinity, E_∞, which can be expressed for any value of the applied

potential as follows:

$$E_\infty(V_a) = n_0 \left(\frac{1}{2} m_i u_{i0}^2 + \frac{1}{2} m_e u_{e0}^2 \right)$$
$$= \frac{1}{2} q n_0 \left(T_i U_{i0} + T_e U_{e0} \right). \qquad (17)$$

When $V_a = V_0$, as $U_{i0} = U_{e0} = 1$, (17) gives

$$E_\infty(V_0) = E_0 = \frac{1}{2} q n_0 \left(T_i + T_e \right). \qquad (18)$$

Taking the energy difference $E_\infty(V_a) - E_\infty(V_0)$ we obtain:

$$E_\infty(V_a) - E_\infty(V_0) = \frac{1}{2} q n_0 \left[T_i(U_{i0} - 1) + T_e(U_{e0} - 1) \right]. \qquad (19)$$

Then the criterion (15) can be interpreted as follows: $E_\infty(V_0)$ corresponds to a minimum of required convective kinetic energy density at infinity. For any other value of V_a the required kinetic energy density can only increase. Consequently, a saturation of criterion (15), i.e. taking $T_i(U_{i0} - 1) + T_e(U_{e0} - 1) = 0$, corresponds to a minimization of $E_\infty(V_a)$ which then takes the constant value $E_0 = \frac{1}{2} q n_0 (T_i + T_e)$ for any applied potential V_a.

Furthermore, it can be verified from (27) that, by saturating (15), the electrical field intensity at the wall is minimized, and therefore that the total charge in the wall-perturbed region is also minimized. Hence the saturation of the general criterion (15) corresponds to the minimal perturbation to the plasma by the biased wall. On the basis of these arguments we postulate the criterion (15) to be always saturated. But then what determines the partition of the constant convective kinetic energy density E_0 between ions and electrons?

To clarify this question we consider the $V_a \leq V_0$ case. Saturating (15), U_{i0} can be expressed as a function of U_{e0}:

$$U_{i0} = 1 + \frac{T_e}{T_i} (1 - U_{e0}). \qquad (20)$$

From (12), U_{e0} is constrained to lie in an interval $[0, U_{e0}^{\max}]$. From (20) it is obvious that in order to minimize the ion initial velocity one should maximize U_{e0} and take $U_{e0} = U_{e0}^{\max}$. By doing so, the electron convective velocity at the wall is implicitly set to $u_{\mathrm{th}e}$ for any value of the applied potential $V_a \leq V_0$, and not only for $V_a = V_0$ when it must be so. One could question the choice of minimizing the initial velocity of the field-accelerated species at the expense of the field-repelled one. The problem can also be stated as follows: The repelled species is adsorbed at the wall by sole virtue of its random thermal motion, which does not depend on the bias potential in the framework of an isothermal model. We know from our solution that the convective velocity for both species must be $u_{\mathrm{th}s}$ in the field-free situation. It should then remain $u_{\mathrm{th}s}$ for any value of V_a as long as the considered species is repelled.

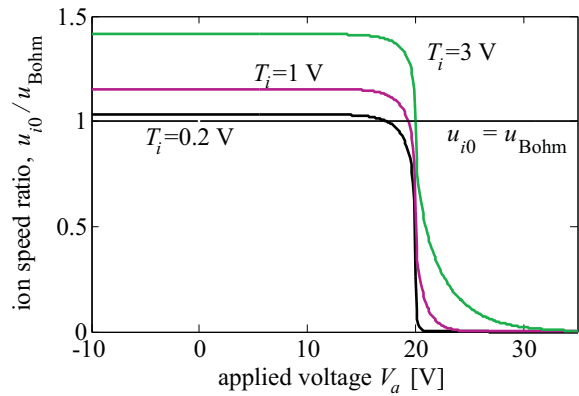The evolution of the initial ion velocity as a function of V_a, in comparison with the Bohm velocity, is shown

FIG. 3. Evolution of the initial ion velocity u_{i0}, normalized to the Bohm velocity, for the infinite plane probe for three different values of the ion temperature T_i. Fixed parameters: Argon gas, $n_0 = 10^{17}$ m^{-3}, $T_e = 3$ V, $V_0 = 20$ V.

on Fig. 3 for three different ion temperatures. It then appears that taking the Bohm velocity as an initial velocity for ions is an acceptable approximation for low T_i and large negative biasing.

To resume the 1D Cartesian result, we first remind that α_e and α_i, from (10), are given by:

$$\alpha_e = -U_{e0} e^{-U_{e0} - \frac{2(V - V_0)}{T_e}},$$
$$\alpha_i = -U_{i0} e^{-U_{i0} + \frac{2(V - V_0)}{T_i}}.$$

The 1D Cartesian moment equations for $V_a \leq V_0$ are finally reduced to

$$U_e = -W_0 \left[\alpha_e \right] \quad \text{and} \quad U_i = -W_{-1} \left[\alpha_i \right],$$
$$\text{where} \quad U_{i0} = 1 + \frac{T_e}{T_i} (1 - U_{e0}), \quad \text{and}$$
$$U_{e0} = -W_0 \left[-e^{\frac{2(V_a - V_0)}{T_e} - 1} \right]. \qquad (21)$$

The electron fluid velocity at the wall is always equal to the thermal velocity $u_{\mathrm{th}e}$. The corresponding loci of the electron and ion fluid velocities are shown on a Lambert function diagram in Fig. 4.

For $V_a \geq V_0$, the roles of electrons and ions are exchanged, accounting for charge sign:

$$U_e = -W_{-1} \left[\alpha_e \right] \quad \text{and} \quad U_i = -W_0 \left[\alpha_i \right],$$
$$\text{where} \quad U_{e0} = 1 + \frac{T_i}{T_e} (1 - U_{i0}), \quad \text{and}$$
$$U_{i0} = -W_0 \left[-e^{-\frac{2(V_a - V_0)}{T_i} - 1} \right]. \qquad (22)$$

C. Wall current-voltage characteristics

Now that U_{i0} and U_{e0} are known, the current per unit area collected at the wall according to this 1D Cartesian
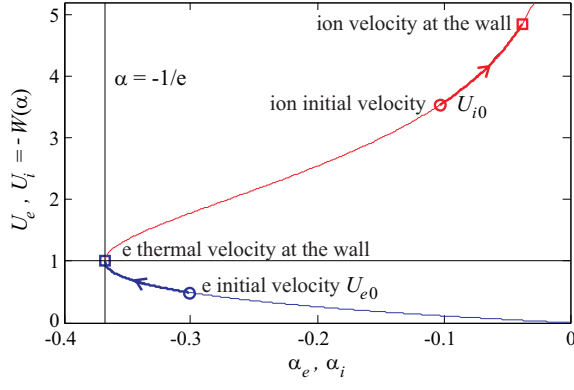
FIG. 4. Locus of the electron normalized square fluid velocity U_e along part of the Lambert branch W_0 (blue line), and the corresponding ion locus (red line) on the Lambert branch W_{-1}, for the case $V_a \leq V_0$ of an infinite plane wall. The y axis is inverted with respect to Fig. 2. Non-typical parameters were used here for clear presentation: $V_0 = 20$ V, $V_a = 19.9$ V, $T_e = 1$ V, and $T_i = 0.2$ V.

solution can be calculated using

$$J_{\text{wall}} = q n_0 (u_{i0} - u_{e0}). \tag{23}$$

The current-voltage (IV) characteristic is a continuous solution as shown in Fig. 5, for an arbitrary set of plasma parameters. The ion and electron currents show very pronounced saturation for $V_a \ll V_0$ and $V_a \gg V_0$ respectively, as expected for an infinite plane probe.[1,2] The plasma parameters were chosen as follows: The pressure of ~ 1 Pa (estimated in Section I.B) is characteristic of low temperature, non-equilibrium plasmas, for which $T_e \sim 3$ V is a typical value imposed by particle balance.[28] The ion temperature is generally above ambient temperature (0.025 V), and a relatively high value, $T_i = 0.2$ V, was chosen here to show its effect in the figures. The plasma density, $n_0 \sim 10^{17}$ m^{-3} corresponds to a representative degree of ionisation $n_0/n_{\text{gas}} \sim 10^{-4}$, and the electron Debye length $\lambda_{De} = (\varepsilon_0 T_e/(n_0 q))^{1/2}$ is 0.04 mm. The plasma potential, $V_0 = 20$ V, is an arbitrary reference level chosen here so that the floating potential V_f is not far from 0 V, because the sheath voltage at a floating probe is often not very different from the sheath voltage at the ground electrode.[28] Figures can be re-calculated for other plasma parameters by using the analytical expressions given in the text.

The influence of T_i on the value of the electron saturation current and on the shape of the IV characteristic around $V_a = V_0$ is illustrated in Fig. 6. The curve for $T_i = T_e$ is later compared with a numerical result of Parrot $et\ al$,[36] in the limit of probe radius much larger than the sheath thickness, in Fig. 15.

The expression for the floating potential V_f of the wall is deduced by setting $J_{\text{wall}} = 0$ in (23):

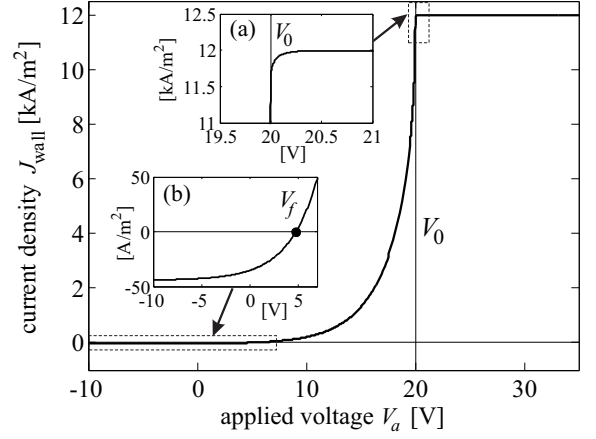$$V_f^{\text{wall}} = V_0 - \frac{T_e}{2} \left(\ln A + 1/A - 1 \right), \tag{24}$$

FIG. 5. Typical current-voltage characteristic for the infinite plane probe predicted by the Lambert solution, using (23). Insets show details (a) around the plasma potential V_0, where the curvature depends on T_i; and (b) around the floating potential V_f. Fixed parameters: Argon gas, $V_0 = 20$ V, $n_0 = 10^{17}$ m^{-3}, $T_i = 0.2$ V, $T_e = 3$ V.
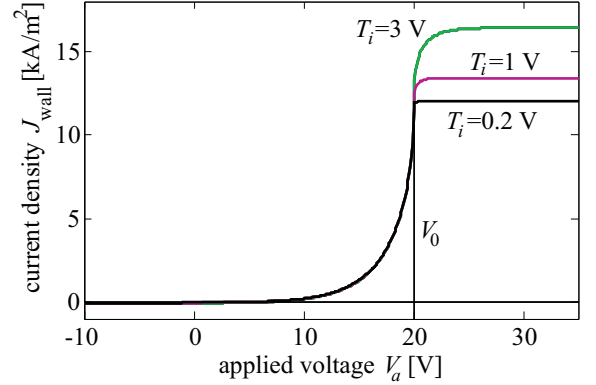

FIG. 6. Current-voltage characteristics for the infinite plane probe for three different values of the ion temperature T_i, using (23). Fixed parameters: Argon gas, $n_0 = 10^{17}$ m^{-3}, $T_e = 3$ V, $V_0 = 20$ V.

where $A = \frac{T_e(m_i + m_e)}{m_e(T_e + T_i)}$.

D. Potential and electric field

The ultimate step for a complete solution would be to obtain the spatial profiles by integrating Poisson's equation,

$$\partial_x^2 V = -\frac{q}{\varepsilon_0}(n_i - n_e). \tag{25}$$

To our knowledge, an analytical solution cannot be found, but at least the square electric field intensity $E^2 = (-\partial_x V)^2$ can be expressed everywhere by the following calculation:

Multiplying (25) by $\partial_x V$ gives

$$\partial_x V \partial_x^2 V = \frac{1}{2}\partial_x[(\partial_x V)^2] = -\frac{q}{\varepsilon_0}(n_i - n_e)\partial_x V. \quad (26)$$

Using the fluid equations for electron and ion momentum (2), and making use of particle conservation ($n_e u_e = n_0 u_{e0} = \phi_e$ and $n_i u_i = n_0 u_{i0} = \phi_i$), we have:

$$m_e\phi_e\partial_x u_e - q n_e\partial_x V + q T_e\partial_x n_e = 0,$$
$$m_i\phi_i\partial_x u_i + q n_i\partial_x V + q T_i\partial_x n_i = 0.$$

By summing these two equations,

$$-q(n_i - n_e)\partial_x V = m_e\phi_e\partial_x u_e + q T_e\partial_x n_e$$
$$+ m_i\phi_i\partial_x u_i + q T_i\partial_x n_i.$$

Then (26) can be directly integrated to find the expression for the square electric field, the integration constant being defined by the limits at infinity:

$$\frac{\varepsilon_0}{2}E^2 = -q T_i(n_0 - n_i) - q T_e(n_0 - n_e)$$
$$- m_i\phi_i(u_{i0} - u_i) - m_e\phi_e(u_{e0} - u_e). \quad (27)$$

Equations (25) or (27) can be integrated numerically starting from a point supposed far enough from the wall so that we can take as initial conditions $n_e = n_i = n_0$, $U_i = U_{i0}$, $U_e = U_{e0}$, and $V = V_0$. An initial infinitesimal gradient for V is imposed and the spatial evolution of the potential is computed until the condition $V = V_a$ is satisfied, which corresponds to the wall. Alternatively, since we know the electric field at the wall surface from (27), we can also integrate Poisson's equation starting from the wall. Both methods give the same result, although the integration starting from the wall tends to diverge and needs much smaller integration steps. For examples, plots of computed profiles for V_a lower, and greater, than V_0 are shown in Figs. 7(a) and (b), respectively. The ion-rich perturbed region in Fig. 7(a) is several Debye lengths wide, but much smaller than the mean free path λ_c, which is characteristic of a collisionless thin sheath for a classical Langmuir probe.[47] The electron-rich perturbation in Fig. 7(b) is narrower and more similar to the Debye length. In Fig. 7(a), the ion initial convective velocity is slightly greater than the Bohm velocity (see Fig. 3 for $V_a = 15$ V), and the electron convective velocity at the wall equals their thermal velocity[35] as discussed in Section II B. Note that the electron initial convective velocity in the $V_a > V_0$ case is slightly higher than their thermal velocity u_{the}, as shown also by Scheiner et al.[31]

E. Discussion of the 1D infinite plane wall case

As already emphasized, the 1D Cartesian collisionless example above, corresponding to an infinite plane wall and a semi-infinite plasma, clearly does not apply to the physical case of a real probe immersed in a plasma.[1] The wall acts more like an electrode than a probe in this case, and a pre-sheath must be considered.[11,12,30] The
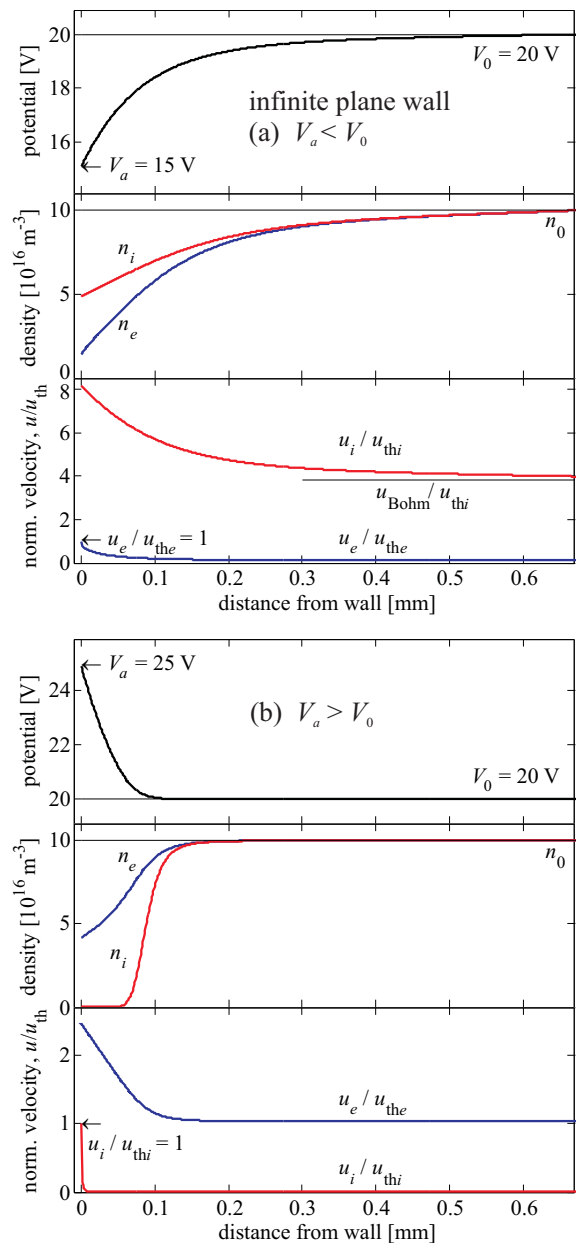

FIG. 7. Potential profile adjacent to an infinite plane wall, ion and electron densities, and velocities normalized by their thermal velocity (692 m/s and $7.26\cdot10^5$ m/s respectively), (a) for $V_a = 15$ V $< V_0 = 20$ V; and (b) for $V_a = 25$ V $> V_0 = 20$ V. Same plasma parameters as for Fig. 5.

fundamental drawback of this 1D Cartesian collisionless solution is that conservation of particle flux requires a non-zero convective velocity plasma source from infinity (Fig. 1(a)), whereas for real finite-sized bodies, particle flux conservation imposes a limit of zero convective velocity from infinity (Fig. 1(b)), as will be shown in the next section. In many conventional 1D models, conditions for finite-sized bodies are nevertheless imposed at infinity ($n_s = n_0$, $V = V_0$, $U_s = 0$), and as such, the 1D Cartesian particle conservation is violated, unless ionization is

included in a collisional pre-sheath.[6] As a consequence there is an artificial separation of space into a collisionless sheath, with a 1D Cartesian constant particle flux, and a collisional pre-sheath where the flux is increasing up to the sheath entrance (Fig. 1(c)), with considerable difficulties to match the two solutions. This problem is considered further in section V in the framework of the big radius probe approximation.

III. 1D RADIAL GEOMETRY FOR CYLINDRICAL PROBES

For radial symmetry, the fluid equations for electron and ion momentum are found to be identical to the 1D Cartesian situation (3):

$$\frac{1}{2}\partial_r U_e - \frac{1}{T_e}\partial_r V + \partial_r \ln(n_e) = 0,$$
$$\frac{1}{2}\partial_r U_i + \frac{1}{T_i}\partial_r V + \partial_r \ln(n_i) = 0. \qquad (28)$$

In cylindrical geometry, however, the steady state radial particle flux conservation is expressed as $\frac{1}{r}\partial_r(r n_s u_s) = 0$, hence

$$2\pi r n_e u_e = \Gamma_e, \quad \text{and} \quad 2\pi r n_i u_i = \Gamma_i, \qquad (29)$$

where $\Gamma_{e,i}$ is the constant particle flux per unit length of the probe, for electrons and ions respectively. As for the 1D Cartesian case, we set at infinity an equal density n_0 for electrons and ions, and the plasma potential V_0. This being stated, it is clear from (29) that both electron and ion fluid velocities must tend toward zero as r tends toward infinity to ensure a finite flux (see Fig. 1(b)). Then, the integration of (28), making use of the boundary conditions at infinity, leads to

$$n_e = n_0 \exp\left(\frac{-U_e}{2} + \frac{V - V_0}{T_e}\right),$$
$$n_i = n_0 \exp\left(\frac{-U_i}{2} - \frac{V - V_0}{T_i}\right). \qquad (30)$$

Because the fluxes $\Gamma_{e,i}$ can no longer be defined by boundary conditions at infinity, we use instead a definition at the cylindrical probe surface located at $r = R_p$:

$$2\pi R_p n_{ea} u_{ea} = \Gamma_e, \quad \text{and} \quad 2\pi R_p n_{ia} u_{ia} = \Gamma_i, \quad (31)$$

u_{ea} and u_{ia} being the electron and ion fluid velocities at the probe and n_{ea} and n_{ia} the corresponding densities according to (30), with the potential of the probe being defined as V_a. We further redefine the normalized square velocities at the probe as

$$U_{ea} = \left(\frac{u_{ea}}{u_{\text{the}}}\right)^2 \quad \text{and} \quad U_{ia} = \left(\frac{u_{ia}}{u_{\text{thi}}}\right)^2. \qquad (32)$$

Then the combination of (29) to (32) leads to the solutions for the square velocities U_e and U_i, which take the following forms:

$$U_e = -W\left[-\frac{R_p^2 U_{ea}}{r^2}e^{-U_{ea} + \frac{2(V_a - V)}{T_e}}\right] = -W[\alpha_e],$$
$$U_i = -W\left[-\frac{R_p^2 U_{ia}}{r^2}e^{-U_{ia} - \frac{2(V_a - V)}{T_i}}\right] = -W[\alpha_i]. (33)$$

As in the 1D Cartesian case, both U_e and U_i are real and positive, so they can only be described by the W_0 and W_{-1} branches of the Lambert function, and $\alpha_{e,i}$ must lie in the interval $[-\frac{1}{e}, 0]$. We still assume for this radial case a monotonic variation of the electric potential with r. In the 1D Cartesian geometry, the monotonicity of $V(x)$ implies the monotonicity of the Lambert function arguments $\alpha_{e,i}(x)$, so that the analysis of the conditions $\alpha_{e,i}(x) \in [-\frac{1}{e}, 0]$ concerns only the boundary conditions at infinity and at the wall surface, as shown in Appendix A. In cylindrical geometry this is no longer true, because of the direct dependence on r of $\alpha_{e,i}(r)$. In fact, taking the spatial derivative of α_e and α_i one finds:

$$\partial_r \alpha_e = \frac{-2\alpha_e}{T_e}\left(\frac{T_e}{r} + \partial_r V\right),$$
$$\partial_r \alpha_i = \frac{-2\alpha_i}{T_i}\left(\frac{T_i}{r} - \partial_r V\right). \qquad (34)$$

To understand the meaning of this, we focus in the following on the $V_a < V_0$ case. Upon the monotonicity hypothesis, the potential continuously increases with r so that $\partial_r V > 0$. For electrons, (34) never vanishes for $\partial_r V > 0$ and the argument $\alpha_e(r)$ is still monotonic. As in the 1D Cartesian model, the condition $\alpha_e \in [-\frac{1}{e}, 0]$ implies that the electron convective velocity at the probe lies in the interval $[0, u_{\text{the}}]$. We have shown in the 1D Cartesian Section II.B that taking $u_{ea} = u_{\text{the}}$ corresponds to a minimal perturbation to the plasma by the biased wall. We postulate in the following that this remains true in radial geometry, or, in other words, that the adsorption mechanism of the repelled species at the probe does not depend on the geometry considered. Then, setting $u_{ea} = u_{\text{the}}$ the electron density at the probe surface is known using (30):

$$n_{ea} = n_0 e^{-\frac{1}{2}} e^{\frac{V_a - V_0}{T_e}}. \qquad (35)$$

For ions, according to (34) the argument α_i reaches its minimum at a radius R_S for which $[\partial_r V]_{R_S} = T_i/R_S$. Consider then the ion velocity evolution (33) starting from infinity toward the probe, as shown schematically in Fig. 8. For large r, U_i tends toward zero and can then only be represented by the first branch of Lambert functions, W_0. Approaching the probe, α_i decreases, and the ion velocity increases up to the minimum of α_i when $r = R_S$. Beyond this point, as α_i now increases, the ion velocity would decrease if it were to remain represented by W_0. As, on the contrary, we expect the ion velocity to continuously increase even for $r < R_S$, this implies that the solution must switch to the second Lambert branch,
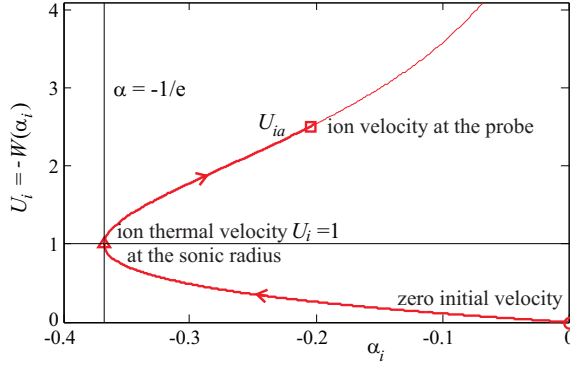
FIG. 8. Locus of the ion normalized square fluid velocity for the case $V_a \leq V_0$ of a cylindrical probe, showing the zero initial velocity (circle), the ion thermal velocity at the sonic radius (triangle), and the ion velocity at the probe (square). The y axis is inverted with respect to Fig. 2. The locus of the electron velocity (not shown) also begins at the origin and traverses the branch W_0, but ends on the probe at the electron thermal velocity, point $[-\frac{1}{e}, 1]$.

W_{-1}. However, to ensure a continuous solution, the continuity between the two branches W_0 and W_{-1} must be satisfied at $r = R_S$. This can only be achieved by setting $\alpha_i(R_S) = -\frac{1}{e}$, which implies that the ion convective velocity at R_S must be $u_{\mathrm{th}i}$. R_S can then be defined as the ion sonic radius (this is not the same as the ion acoustic speed associated with Bohm's velocity). Clearly, for probe theories with cold ions ($T_i = 0$), the ion sonic radius could have no meaning.

An interesting question arises when the applied potential V_a approaches V_0. Clearly, for the field-free case $V_a = V_0$, a sonic radius R_S can no longer be defined because $\partial_r V = 0$ everywhere. Then, there must be a limit value $V_a = V_{\mathrm{lim}}$ for which R_S coincides with R_p, implying that the ion convective velocity at the probe is $u_{\mathrm{th}i}$ for this case. Above V_{lim} the ion convective velocity could be thought to fall below $u_{\mathrm{th}i}$. On the other hand, according to the 1D Cartesian solution, for the field-free situation ($V_a = V_0$) we expect the ion and electron convective velocities at the probe to be $u_{\mathrm{th}i,\mathrm{th}e}$, and we have indeed already postulated that this remains true in the radial case by setting $u_{ea} = u_{\mathrm{th}e}$ above. This then implies that the convective velocities of ions and electrons in the zone between the two limit potentials V_{lim} (one for $V_a < V_0$ when $[\partial_r V]_{R_p} = T_i/R_p$, and one for $V_a > V_0$ when $[\partial_r V]_{R_p} = -T_e/R_p$) are to be constant at $u_{\mathrm{th}i}$ and $u_{\mathrm{th}e}$, respectively.

Under this assumption, in this "constant velocity zone", both ion and electron densities at the probe are known, using (30), and can be expressed for any probe radius R_p as:

$$n_{ea} = n_0 e^{-\frac{1}{2}} e^{\frac{V_a - V_0}{T_e}},$$
$$n_{ia} = n_0 e^{-\frac{1}{2}} e^{-\frac{V_a - V_0}{T_i}}. \tag{36}$$
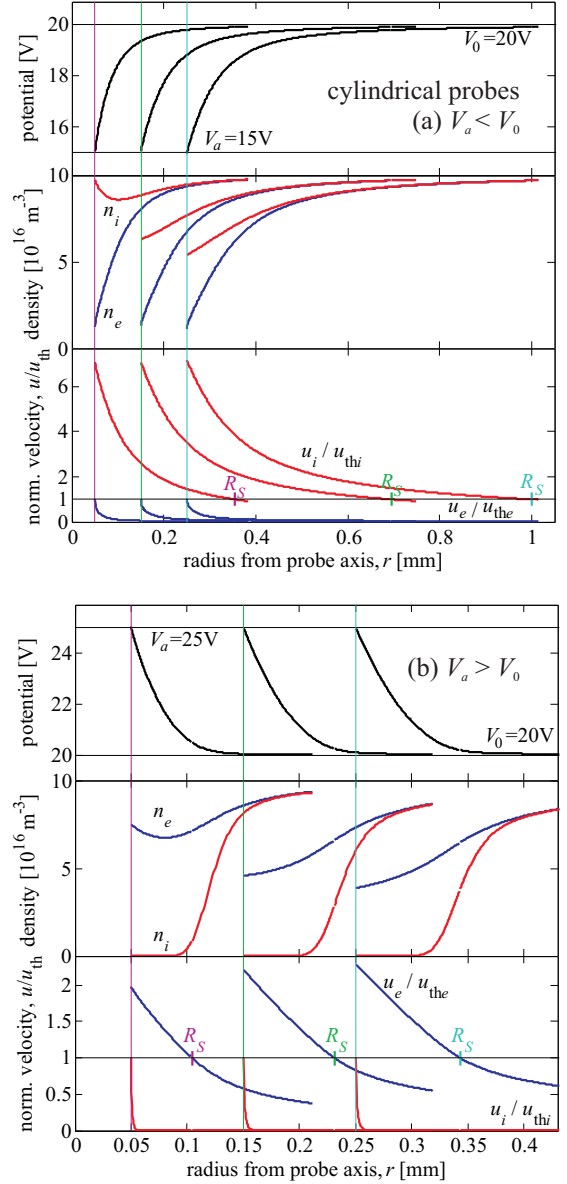
Going back to the more general case for which an ion

FIG. 9. Cylindrical probe 1D radial profiles of potential, density, and convective velocity normalized to the thermal velocity, (a) for probe voltage $V_a = 15$ V $< V_0 = 20$ V, and (b) for probe voltage $V_a = 25$ V $> V_0 = 20$ V, for three cylindrical probe radii $R_p = 0.05$, 0.15 and 0.25 mm (indicated by the vertical lines). The ion sonic radius R_S in (a), and the electron sonic radius R_S in (b), is also shown for each probe. Fixed parameters: Argon gas, $n_0 = 10^{17}$ m^{-3}, $T_i = 0.2$ V, $T_e = 3$ V.

sonic radius can be defined ($V_a < V_{\mathrm{lim}} < V_0$), the electron convective velocity at the probe ($r = R_p$) being known to be $u_{\mathrm{th}e}$, and the ion convective velocity at the sonic radius ($r = R_S$) to be $u_{\mathrm{th}i}$, we can rewrite (33) to obtain:

$$U_e = -W_0 \left[-\frac{R_p^2}{r^2} e^{\frac{2(V_a - V)}{T_e} - 1} \right],$$

$$U_i = -W_0 \left[-\frac{R_S^2}{r^2} e^{\frac{-2(V_S - V)}{T_i}} - 1 \right], \quad V \geq V_S,$$

$$U_i = -W_{-1} \left[-\frac{R_S^2}{r^2} e^{\frac{-2(V_S - V)}{T_i}} - 1 \right], \quad V \leq V_S. \quad (37)$$

V_S is the value of the electric potential at the sonic radius R_S, and both parameters are to be determined. Recalling that these are defined by the following conditions on the electric potential:

$$[\partial_r V]_{R_S} = \frac{T_i}{R_S}, \quad \text{and} \quad V(R_S) = V_S, \quad (38)$$

and that in 1D radial coordinates Poisson's equation takes the form:

$$\frac{1}{r} \partial_r (r \partial_r V) = \frac{1}{r} \partial_r V + \partial_r^2 V = -\frac{q}{\varepsilon_0} (n_i - n_e), \quad (39)$$

R_S and V_S can be determined by requiring that the solution of Poisson's equation satisfies the boundary conditions:

$$V(R_p) = V_a, \quad \text{and} \quad V(r \to \infty) = V_0.$$

As far as we know, no analytical solution for Poisson's equation can be found, as also in the 1D Cartesian case, and we have to perform numerical integrations starting from R_S. If the correct pair (R_S, V_S) is used as initial conditions, the integration of (39) towards the probe surface (decreasing r) will respect the boundary condition $V(R_p) = V_a$, while the integration towards infinity (increasing r) must lead to the limiting value V_0. The potential profile can then be computed iteratively (see Appendix B 2) in order to simultaneously satisfy these two boundary conditions. Note that, apart from a numerical determination, the value for V_S can be analytically restricted to quite narrow intervals on the basis of simple arguments concerning the charge density and the density gradients at $r = R_S$, as shown in Appendix B 1.

As a first illustrative result we show on figures 9(a) and (b) the ion and electron density profiles computed for a same value of applied potential V_a ($V_a < V_0$ for figure 9(a) and $V_a > V_0$ for (b)), for three probe radii. We first remark that, although the probe radii vary from 0.05 mm to 0.25 mm, the widths of the ion-rich perturbation in Fig. 9(a) are all several Debye lengths thick. This is much narrower than the mean free path λ_c, and is characteristic of a collisionless thin sheath for a classical Langmuir probe,[47] qualitatively similar to the 1D Cartesian case in Fig. 7(a). The electron-rich perturbation in Fig. 9(b) is again narrower and more similar to the Debye length. It is generally found that the sonic distance $(R_S - R_p)$ increases with increasing probe radius.

A second observation concerns the non-monotonic ion density profiles on figure 9(a) which appear for small probe radius and which are expected according to previous works, notably Laframboise.[32] Note that the profiles of voltage and convective velocity remain monotonic, even when the charge densities are not. It is shown here that the same effect is expected for electrons (figure 9(b))
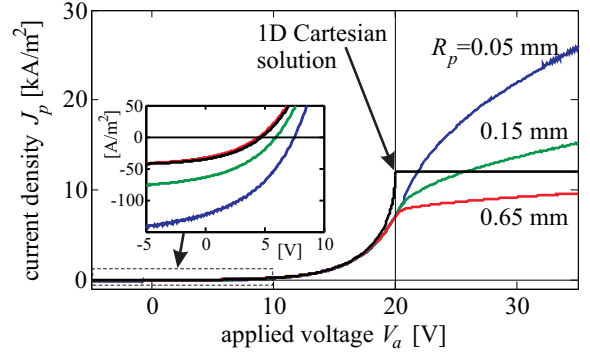

FIG. 10. Current density-voltage characteristics for three cylindrical probe radii, $R_p = 0.05, 0.15$ and 0.65 mm, and for the 1D Cartesian solution from Fig. 5. The inset shows the ion non-saturation and floating potentials. Fixed parameters: Argon gas, $n_0 = 10^{17}$ m^{-3}, $T_i = 0.2$ V, $T_e = 3$ V, $V_0 = 20$ V.

when $V_a > V_0$. It should also be noted that the charge separation at the ion sonic radius R_S is very small (typically 0.01-0.1%) for $V_a < V_0$, and this remains true up to values of V_a very close to V_0. On the other hand, when $V_a > V_0$ the charge separation at the electron sonic radius R_S is large (typically 50%) even for large positive bias. It then appears that if the ion sonic radius R_S could be thought of as a possible definition of a quasi-neutral sheath edge in the $V_a < V_0$ case (at least for $V_a \ll V_0$), it is not generalizable to the $V_a > V_0$ case.

A. IV characteristics for cylindrical probes

Figure 10 shows the predicted IV characteristics for three different probe diameters. The results are presented as collected current per unit area (A/m^2) for comparison. The noise in the characteristics, especially for the smallest probe, is due to the numerical resolution of R_S. The first important result concerns the observation of non-saturating electron and ion currents. The two-fluid solution presented here accounts for this experimental fact, which arises due to an increase in R_S (Appendix B 3), without reference to orbital-motion-limited (OML) theory.[2,19,21,27,48–50] Furthermore, the non-saturation is more pronounced for small probe radii, also as observed.[32] The floating potential depends on the probe radius, as can be seen in the inset. It can generally be expressed as

$$V_f^{\text{cyl}} = V_0 - \frac{T_e}{2} \ln \left[\frac{m_i}{m_e} \frac{T_e}{T_i} \frac{R_p^2}{R_S^2} e^{\frac{2(V_S - V_0)}{T_i}} \right]. \quad (40)$$

Fig. 10 also shows the IV characteristic predicted by the 1D Cartesian solution from Fig. 5. Clearly, the large cylindrical probe characteristic (for example, $R_p = 0.65$ mm in Fig. 10) does not seem to tend toward the 1D Cartesian result as could be expected. This
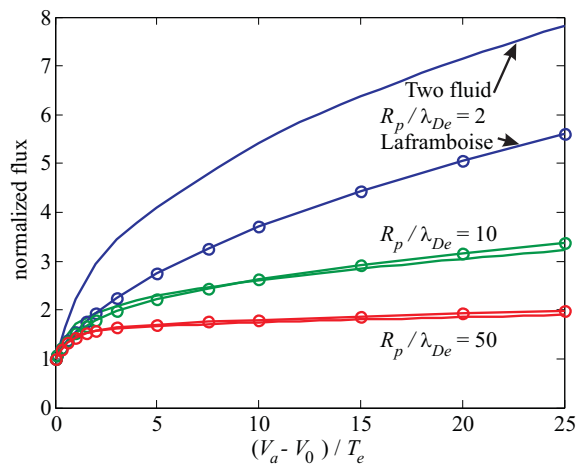
FIG. 11. Comparison between the present model and graphical results of Laframboise[32] (Fig. 39), for the flux of attracted species (normalized to the value at the plasma potential V_0) *vs* the dimensionless probe potential $(V_a - V_0)/T_e$. Lines and circles for the Laframboise results; plain lines for the present model. Results are shown for three ratios of probe radius to electron Debye length, $R_p/\lambda_{De} = 2, 10, 50$, calculated for $T_e = T_i = 3$ V.

contradiction will be explained in Section V in the framework of the big radius probe approximation.

Figure 11 shows the flux of attracted species calculated for the special case $T_i = T_e$, in order to compare with graphical results of Laframboise.[32] The agreement is good for the larger probes (probe radius to electron Debye length, $R_p/\lambda_{De} = 10, 50$), although the non-saturation for the small probe ($R_p/\lambda_{De} = 2$) is more pronounced for the present model.

In order to fully exploit this radial solution for the analysis of measured characteristics, one has to know the dependence of the sonic radius R_S and of the sonic potential V_S with the applied voltage V_a. However, we show in Appendix B 4 how the main plasma parameters, n_0 and T_e, can be conveniently extracted from experimentally-measured characteristics, upon the assumption of a constant ion current contribution between floating and plasma potentials.

IV. 1D RADIAL GEOMETRY FOR SPHERICAL PROBES

The analysis of the spherical probe can be carried out by following the same method as for the cylindrical probe. The 1D radial expressions are similar and one has just to perform a $r \rightarrow r^2$ substitution to switch from the cylindrical case to the spherical one. Attention has nevertheless to be paid to the fact that the sonic radius R_S is now defined by the relation:

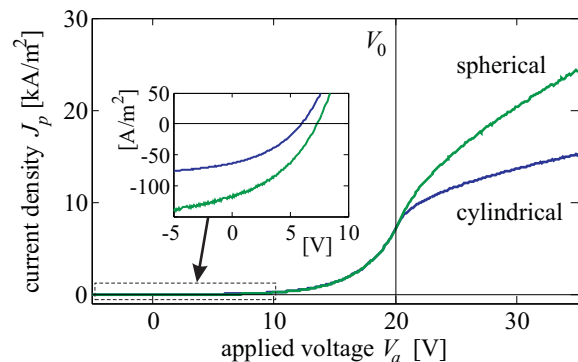$$[\partial_r V]_{R_S} = \pm \frac{2T_{i,e}}{R_S}. \tag{41}$$

FIG. 12. Current density-voltage characteristics predicted for a cylindrical and a spherical probe, both with radius $R_p = 0.15$ mm. The inset shows the ion non-saturation and floating potentials. Fixed parameters: Argon gas, $n_0 = 10^{17}$ m^{-3}, $T_i = 0.2$ V, $T_e = 3$ V, $V_0 = 20$ V.

Figure 12 shows the IV characteristics (current per unit area) predicted for a cylindrical probe ($R_p = 0.15$ mm) and a spherical probe of same radius. It can be seen that the non-saturation of spherical probes is more pronounced than for cylindrical ones, as seen in experimental observation and numerical results.[32]

V. 1D RADIAL GEOMETRY IN THE LIMIT OF BIG RADIUS PROBES

Intuitively, the cylindrical 1D radial solution should tend toward the 1D Cartesian solution when the probe radius R_p becomes very large compared to the perturbed region. It can be seen on figure 10 that when the probe diameter is increased the IV characteristic becomes more and more saturated for large biasing, as expected. However, the values of the ion and electron saturation currents are higher for the 1D Cartesian solution than for the cylindrical one with large R_p. This apparent contradiction arises from an incompatibility between the boundary conditions taken for the velocities at infinity in the two geometries, which can be explained as follows:

For both models, an equal density n_0 for ions and electrons and a uniform electric potential V_0 can certainly be imposed at infinity. The difference then comes from the particle conservation equations

$$n_s u_s = \phi_s \quad \text{for 1D Cartesian,}$$
$$2\pi r n_s u_s = \Gamma_s \quad \text{for 1D cylindrical.}$$

At infinity, where $n_s = n_0$, u_s cannot vanish for the 1D Cartesian case because the constant particle flux densities ϕ_s must be non-zero (Fig. 1(a)). On the other hand, to ensure constant, finite values of Γ_s, the velocity must tend to zero at infinity in the cylindrical situation (Fig. 1(b)). Therefore, in the limit of large R_p, the 1D Cartesian result can never be recovered because, however large the probe radius, the initial velocities at infinity must be zero. Another consequence of vanishing initial

velocities is that the particle densities at the probe for $V_a = V_0$ are $n_0 e^{-\frac{1}{2}}$ in the cylindrical analysis (see (35)) and not n_0 as in the 1D Cartesian model.

We therefore focus now on the big radius probe problem. The fluid equations for electron and ion momentum (28) do not depend on R_p and will not be changed in the framework of the large probe approximation. Then equations (30) remain valid:

$$n_e = n_0 \exp\left(\frac{-U_e}{2} + \frac{V - V_0}{T_e}\right),$$

$$n_i = n_0 \exp\left(\frac{-U_i}{2} - \frac{V - V_0}{T_i}\right).$$

Consider now particle conservation in cylindrical 1D radial systems for a distance x above the probe surface:

$$rn_s u_s = (R_p + x)n_s u_s = \frac{\Gamma_s}{2\pi} = R_p n_{sa} u_{sa}, \qquad (42)$$

where n_{sa} and u_{sa} are respectively the density and the velocity of the considered species at the probe surface. If we take the probe radius to be very large with respect to the sheath length scale, then x can be neglected with regard to R_p in (42) and we directly obtain the 1D Cartesian particle conservation law in this limit:

$$n_s u_s = n_{sa} u_{sa} = \phi_s. \qquad (43)$$

Boundary conditions are necessary to solve the problem as in the 1D Cartesian section, but x cannot extend to infinity in the framework of this approximation. Instead, we have to state an upper boundary for our solution at a given position $x_{sh} \ll R_p$. The only condition we will require at this radius is an equal density n_{sh} for ions and electrons, by analogy with the sheath defining the boundary of quasi-neutrality with respect to the pre-sheath in conventional models.[5,11,12] By doing so, we employ the classical notions of sheath and pre-sheath, but it has to be noted that conditions other than quasi-neutrality at the sheath edge could, or even should, be envisaged.

A. The sheath in the limit of big radius probes

The potential at x_{sh} is set to be V_{sh} while the initial electron and ion velocities at the sheath edge are u_{esh} and u_{ish} (Fig. 1(c)). With these definitions, the combination of (30) and (43) gives the solutions

$$U_e = -W\left[-\frac{n_{sh}^2}{n_0^2} U_{esh} e^{-\frac{2(V-V_0)}{T_e}}\right],$$

$$U_i = -W\left[-\frac{n_{sh}^2}{n_0^2} U_{ish} e^{\frac{2(V-V_0)}{T_i}}\right], \qquad (44)$$

where we have reintroduced the normalized initial square velocities $U_{esh} = (u_{esh}/u_{the})^2$ and $U_{ish} = (u_{ish}/u_{thi})^2$. In order to be self-consistent, (44) must lead to $U_e = U_{esh}$
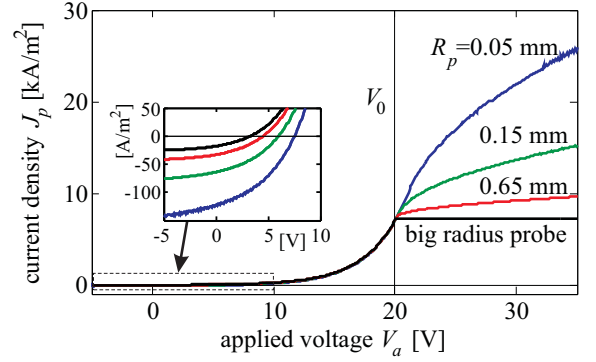

FIG. 13. Current density-voltage characteristics predicted for three different cylindrical probe radii (0.05, 0.15 and 0.65mm) and for the big radius probe approximation. The inset shows the ion non-saturation. Fixed parameters: Argon gas, $n_0 = 10^{17}$ m^{-3}, $T_i = 0.2$ V, $T_e = 3$ V, $V_0 = 20$ V.

and $U_i = U_{ish}$ for $V = V_{sh}$. From these two conditions we obtain

$$V_{sh} = V_0 - \frac{T_e T_i (U_{ish} - U_{esh})}{2(T_e + T_i)}, \qquad (45)$$

$$n_{sh} = n_0 e^{-\frac{T_i U_{ish} + T_e U_{esh}}{2(T_e + T_i)}}. \qquad (46)$$

As in the 1D Cartesian model, we express the condition for a continuous variation of the net charge density at the sheath edge as:

$$[\partial_V Q]_{V_{sh}} = [\partial_V (n_i - n_e)]_{V_{sh}} \leq 0,$$

which according to (30) and (44-46), after some algebra, gives again the general criterion (15):

$$T_i(U_{ish} - 1) + T_e(U_{esh} - 1) \geq 0.$$

Now consider the case for which $V_a < V_0$, the ion-rich sheath. As explained in the 1D Cartesian section, we then take the initial normalized square velocity for electrons U_{esh} to be U_{esh}^{max}, its maximum value. Therefore, taking (15) to be saturated gives

$$U_{ish} = 1 + \frac{T_e}{T_i}(1 - U_{esh}^{max}).$$

Then, according to this expression for U_{ish}, (45) and (46) become

$$V_{sh} = V_0 - \frac{T_e}{2}(1 - U_{esh}^{max}), \qquad (47)$$

$$n_{sh} = n_0 e^{-\frac{1}{2}}, \qquad (48)$$

with

$$U_{esh}^{max} = e^{\frac{2(V_a - V_0)}{T_e}}. \qquad (49)$$

Interestingly, in the framework of this big radius probe approximation, we find the classical result of a potential drop (with regard to plasma potential) at the sheath edge

of approximatively $T_e/2$, at least for V_a sufficiently lower than V_0. We furthermore find that the plasma density at the sheath edge is $n_0 \mathrm{e}^{-1/2}$, which is also a classical result.[27]

For $V_a > V_0$, saturating (15) we get:

$$U_{esh} = 1 + \frac{T_i}{T_e}(1 - U_{ish}^{\max}).$$

This also leads to $n_{sh} = n_0 \mathrm{e}^{-1/2}$, and the potential at the sheath edge becomes

$$V_{sh} = V_0 + \frac{T_i}{2}(1 - U_{ish}^{\max}), \tag{50}$$

with

$$U_{ish}^{\max} = \mathrm{e}^{-\frac{2(V_a - V_0)}{T_i}}. \tag{51}$$

B. IV characteristics in the limit of big radius probes, and comparison with a classical model

The IV characteristic according to the big radius probe approximation is shown on figure 13 in comparison with the IV curves calculated for cylindrical probes with different R_p, which resolves the apparent contradiction noted in Section III A regarding the discrepancy of the 1D Cartesian solution in Fig. 10.

The predictions of this model differ significantly from those of conventional theory,[28] as illustrated on Fig. 14(a). The main reason for these differences arises from the modification of the electron current expression in the two models:

$$J_e^{\mathrm{classical}} = q\frac{n_0}{4}\mathrm{e}^{\left(\frac{V_a - V_0}{T_e}\right)}\sqrt{\frac{8qT_e}{\pi m_e}},$$

$$J_e^{\mathrm{big\ radius}} = qn_0\mathrm{e}^{-\frac{1}{2}}\mathrm{e}^{\left(\frac{V_a - V_0}{T_e}\right)}\sqrt{\frac{qT_e}{m_e}},$$

for $V_a < V_0$, as shown in Fig. 14(b).

The ion current contributions for both models are also represented on figure 14(b). In classical theory, the ion current is taken to be constant for any value of the applied potential, whereas the big probe solution implies a continuously decreasing ion current as V_a approaches, and passes, the plasma potential. This being said, the electron contribution to the total current is much higher than the ion current in this region, so the approximation of a constant ion flux is fairly reasonable. With regard to the ion saturation currents (figure 14(c)), the expressions for the two models can be compared as follows:

$$J_{isat}^{\mathrm{classical}} = -qn_0\mathrm{e}^{-\frac{1}{2}}\sqrt{qT_e/m_i},$$

$$J_{isat}^{\mathrm{big\ radius}} = -qn_0\mathrm{e}^{-\frac{1}{2}}\sqrt{q(T_e + T_i)/m_i},$$

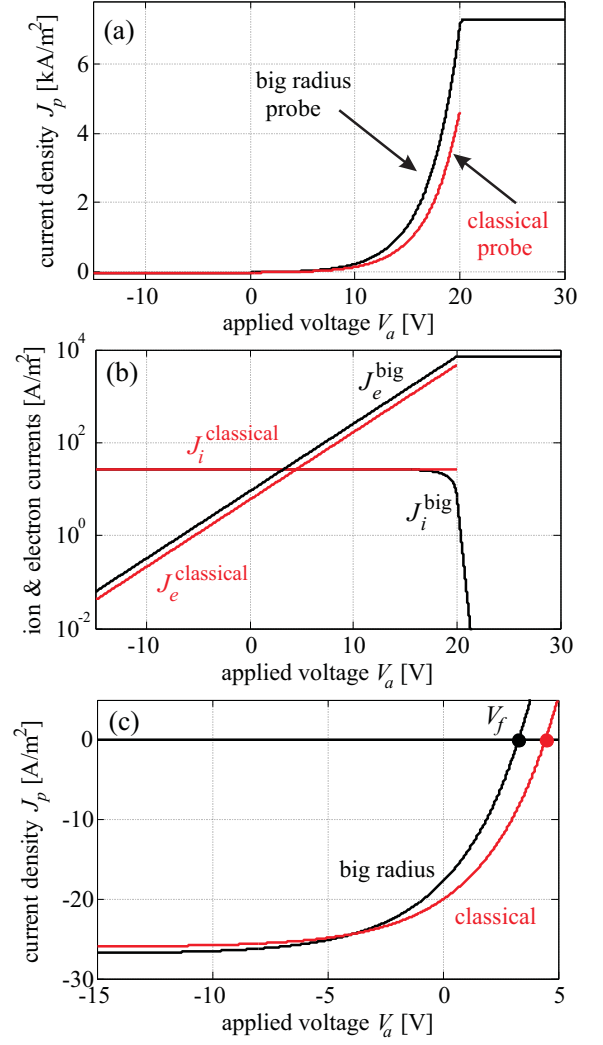where the big radius probe expression accounts for non-zero ion temperature.

FIG. 14. (a) IV characteristics for a classical model (red lines) compared with the big radius probe approximation (black lines); (b) semi-log plot of the electron currents, J_e, and magnitude of the ion currents, J_i; (c) expanded scale to show the ion saturation currents and the floating potentials V_f. Fixed parameters: Argon gas, $n_0 = 10^{17}$ m^{-3}, $T_i = 0.2$ V, $T_e = 3$ V, $V_0 = 20$ V.

The modification of electron and ion flux expressions naturally implies different values for the floating potential:

$$V_f^{\mathrm{classical}} = V_0 - \frac{T_e}{2}\left[\ln(\frac{m_i}{2\pi m_e}) + 1\right] = V_0 - \frac{T_e}{2}\ln\frac{\mathrm{e}^1 m_i}{2\pi m_e},$$

$$V_f^{\mathrm{big\ radius}} = V_0 - \frac{T_e}{2}\ln\frac{T_e(m_i + m_e)}{m_e(T_e + T_i)} \cong V_0 - \frac{T_e}{2}\ln\frac{m_i}{m_e},$$

which differ by $\frac{T_e}{2}\ln(\frac{\mathrm{e}^1}{2\pi}) \cong 0.4 T_e$ as shown in Fig. 14(c).

Finally, Fig. 15 shows the IV characteristic predicted in the framework of the big probe approximation for the special case $T_e = T_i$, in order to compare with the numerical result of Parrot *et al*,[36] also obtained in
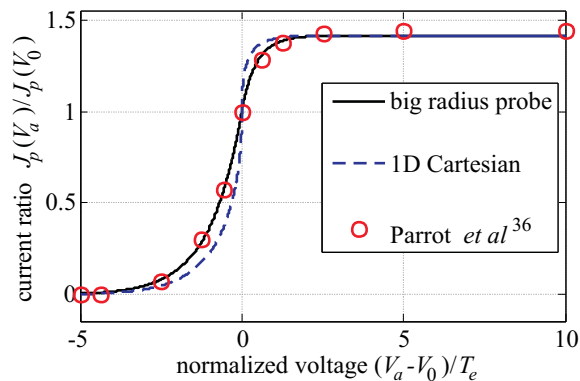
FIG. 15. Normalized current-voltage characteristics for the big radius probe, the 1D Cartesian case, and the numerical simulation of Parrot et al^{36} for the special case of $T_i = T_e$ and ionized oxygen atoms. $n_0 = 10^{17}$ m^{-3}, $T_i = T_e = 3$ V.

the limit of probe radius much larger than the sheath thickness. The correspondence between both curves is excellent and suggests a convergence of both approaches in the big radius probe limit, similarly to Fig. 11. Fig. 15 also shows the IV characteristic for the 1D Cartesian infinite plane wall, which differs from the big radius probe limit due to their different boundary conditions at infinity.

In conclusion, it has been shown that the classical 1D Cartesian model of a collisionless sheath applies only in the limit of large radius cylindrical (or spherical) probes. This is why non-saturation effects observed experimentally for small probes could not be described by the classical sheath model. The big radius probe approximation relies on the supposition that the probe radius is much bigger than the typical length scale of the sheath, or plasma perturbation. We note that, with our set of parameters, this typical length scale is about 1 mm, and therefore a "big probe" would in reality be several centimeters in diameter, and would rather be qualified as a big body.

VI. DISCUSSION

A. Concerning the extension of solutions up to infinity

Clearly, whichever geometry is considered, an infinite plasma has no meaning if ionization is included, because an infinite plasma would generate infinite particle fluxes that would have to be adsorbed by the wall or the immersed body. In such models, a probe must be taken to be immersed in plasma of limited extent, or in other words, enclosed in a vessel. If the probe is small enough to be non-perturbing, the majority of the ionization contributes to fluxes toward external walls. Considering a simplified axisymmetric system in Fig. 16, the flux for a given species is oriented toward the probe in its vicin-
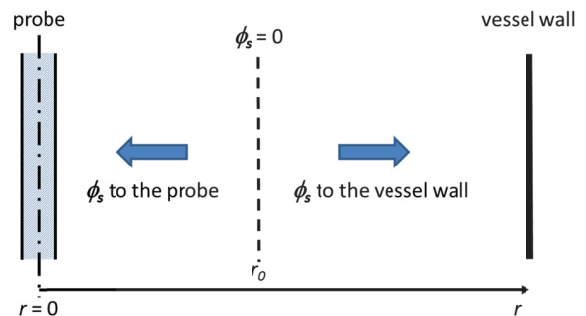

FIG. 16. Schematic of flows to a cylindrical probe and to a cylindrical wall, showing the watershed radius r_0.

ity while it is oriented toward the vessel wall far away from the probe. There is therefore a certain watershed radius r_0 at which the particle flux must vanish.[3] The flux adsorbed by the probe is then given by the integral of all ionizations between the probe radius R_p and r_0. For a given flux to the probe, decreasing the ionization rate leads to increasing r_0, which tends to infinity in the collisionless (ionizationless) limit. As a consequence, the extension of the perturbed region for cylindrical and spherical probes to infinity seems in fact to be required in the framework of collisionless models.

Then, consistent with the collisionless hypothesis, our solution extends from the probe to infinity, without any distinction possible between sheath and pre-sheath because the charge separation evolves continuously over the whole domain. This being said, although the solution is mathematically valid over the whole space, it is not physically valid everywhere: If the collisionless hypothesis is acceptable for low pressure in the vicinity of the probe (i.e. in the "sheath" where the charge separation is significant), over larger distances, collisions are determinant and can no longer be neglected. It should be noted, however, that there is a fundamental difference between 1D Cartesian and radial geometries: In the 1D Cartesian case, a collisional (ionization) presheath is required to justify the flux at the sheath entrance,[6] while for radial probes, the inward flux concentration in the geometric presheath allows a collisionless presheath to relax asymptotically to the unperturbed plasma.[11,12]

B. Concerning the repelled species convective velocity at the probe surface

In the 1D Cartesian demonstration it was shown that the repelled species, s_r, has a convective velocity at the probe surface, $u_{s_r a}$, which is undetermined but must lie in an interval $[0, u_{\mathrm{th}s_r}]$. It was further shown that, in the field free situation, $u_{\mathrm{th}s_r}$ is the only possible value for $u_{s_r a}$ in order to ensure continuous solutions when the bias of the wall crosses the plasma potential. We then extended this result to all bias potentials for the repelled species. By doing so we actually converge with the con-

ventional approach in which the electron flux at the wall surface is taken to be given by the random thermal kinetic flux[1–3,8,9,13,19,26–28,32,43,44] $\frac{1}{4}n_{ea}\bar{v}_e = \frac{1}{\sqrt{2\pi}}n_{ea}u_{\mathrm{th}e}$, at least, for the case $V_a < V_0$. The only difference is the factor $\frac{1}{\sqrt{2\pi}}$ which does not appear in our solution. The classical kinetic theory flux, $\frac{1}{4}n_{ea}\sqrt{\frac{8qT_e}{\pi m_e}}$, applies to the case of non-interacting particles in front of an adsorbing wall: In a kinetic description, the velocity distribution is truncated because no particles return from the wall. The classical kinetic theory result thus corresponds to the flux of a half-Maxwellian velocity distribution. However, in the fluid approach considered here, Maxwellian velocity distributions are assumed to persist up to the adsorbing wall surface. Our solution then self-consistently demonstrates that the predicted net flux convected to the wall, $n_{ea}\sqrt{\frac{qT_e}{m_e}}$, is larger than the classical kinetic theory result by a factor $\sqrt{2\pi}$.

In the cylindrical and spherical 1D radial cases the repelled species velocity at the probe is also found to lie in the interval $[0, u_{\mathrm{th}s_r}]$, but no condition was found for the field free situation. On the contrary, we have demonstrated the existence of a zone in terms of probe bias, in the vicinity of the plasma potential V_0, in which the convective velocities of both repelled and field accelerated species could fall below $u_{\mathrm{th}s}$. Our main question here concerns the application of 1D Cartesian results to cylindrical and spherical 1D radial cases. In fact, to solve the 1D radial problem we postulated that the field-free convective velocity at the probe for the repelled species is also $u_{\mathrm{th}s_r}$, as it must be in the 1D Cartesian situation. By doing so we have in fact made the conventional assumption that the adsorption mechanism of the repelled species at the biased surface does not depend on the geometry considered.

C. The criterion on initial velocities

According to our demonstration, a criterion on initial velocities seems to have no meaning apart from the 1D Cartesian model for which the flux conservation imposes non-vanishing velocities at infinity, or at the sheath edge in the framework of the big radius probe approximation. In 1D Cartesian systems, the criterion on initial velocities arises from the requirement of a continuously-decreasing charge density when going away from the wall, up to infinity or to the sheath edge where electrons and ions have the same density. In 1D radial geometries, all the Lambert function arguments vanish in the limit of large r, and the requirement of a continuously-decreasing charge density up to infinity leads to the trivial condition $1/T_e + 1/T_i \geq 0$. In this case, another criterion is required to determine the charge separation (or, equivalently, the electric potential) at the sonic radius.

VII. CONCLUSIONS

The two-fluid equations were solved using the Lambert function for the 1D cases of planar, cylindrical and spherical Langmuir probes in a steady state, isothermal plasma. Because electron inertia and ion temperature are both included, the fluid equations are symmetric in the terms for electrons and ions, hence the solutions apply below and above the plasma potential. The solution of the fluid equations allows ion and electron densities to be expressed as functions of the electric potential, which is then the only remaining function implied in Poisson's equation. This final differential equation is integrated numerically to obtain the full solution, i.e. the spatial dependence of all parameters. The calculated current-voltage characteristics for radial probes correspond with general experimental observations, such as non-saturation of the ion and electron saturation currents, which are more pronounced for small probe radii. Furthermore, spherical probe currents show stronger non-saturation than cylindrical probes for identical radius.

The model gives a single 1D solution for radial probes extending from the probe surface up to infinity. The connection with classical models considering a separation of space between a 1D Cartesian collisionless sheath and a quasineutral pre-sheath was made, and it was demonstrated that this approach is valid only as an approximation in the framework of big radius probes for which the sheath length scale can be considered to be very small compared to the probe radius. In the limit of big radius probes, the solution leads to several generalized results which converge towards conventional ones provided that proper approximations are applied. Notably, a criterion on initial velocities was derived, generalizing the Bohm criterion, which not only implies a minimal initial velocity for ions entering an ion-rich sheath, but also for electrons when the probe bias is higher than the plasma potential. This unique expression for both species was shown to be related to the total required kinetic energy density of ions and electrons at the sheath entrance. Saturation of the criterion minimizes this energy density, as well as the total charge of the perturbed region; this case then corresponds to the minimum perturbation to the plasma by the probe for any given probe potential.

Another surprising result of the 1D Cartesian solution is the prediction, in the field free situation, of an adsorbed particle flux by the wall that differs from the usually-stated thermal kinetic flux by a factor $\frac{1}{\sqrt{2\pi}}$. This arises from the requirement of continuous solutions when the wall bias potential crosses the plasma potential. As nothing distinguishes a charged particle from a neutral one in the field free situation, this result can in principle be generalized to neutral particle fluxes at an adsorbing surface.
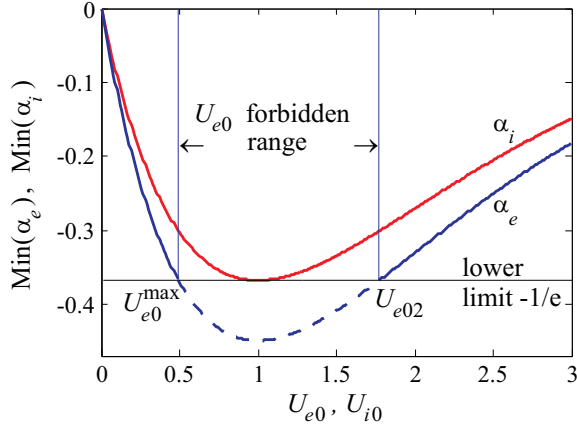
FIG. 17. Minimum values of the Lambert function arguments $\alpha_e(U_{e0}, V_a)$ as a function of U_{e0} (blue curve); and $\alpha_i(U_{i0}, V_0)$ as a function of U_{i0} (red curve), for the case $V_a \leq V_0$. Non-typical parameters are used for clearer presentation: $V_0 = 20$ V, $V_a = 19.9$ V, $T_e = 1$ V, and $T_i = 0.2$ V.

Appendix A: 1D Cartesian solution

The solutions (10) must be real and positive, which implies that the Lambert functions must be real and negative. The reality condition implies that $U_{e,i}$ must be described by the W_0 and W_{-1} branches of Lambert function, and negative values are obtained only provided that the arguments $\alpha_{e,i}$ are restricted to the interval $[-\frac{1}{e}, 0]$. We therefore write:

$$-\frac{1}{e} \leq -U_{e0}e^{-U_{e0} - \frac{2(V-V_0)}{T_e}} = \alpha_e(U_{e0}, V) \leq 0,$$
$$-\frac{1}{e} \leq -U_{i0}e^{-U_{i0} + \frac{2(V-V_0)}{T_i}} = \alpha_i(U_{i0}, V) \leq 0. \quad \text{(A1)}$$

The upper limit is always satisfied and we have only to deal with the lower one. These inequalities must be satisfied for all space, from infinity where $V = V_0$, to the wall where a potential V_a is applied. The solutions depend on whether the probe applied potential V_a is less than, greater than, or equal to the plasma potential V_0. We consider here the case $V_a \leq V_0$, the reasoning for the case $V_a \geq V_0$ being similar with inverted roles for ions and electrons, accounting for charge sign.

The potential V is assumed to vary monotonically with x for any applied potential V_a. Under this condition, for $V_a \leq V_0$, the argument $\alpha_e(U_{e0}, V)$ reaches its minimum at the wall where $V = V_a$, for any value of U_{e0}. On the other hand, for any U_{i0}, the minimum value for $\alpha_i(U_{i0}, V)$ is reached at infinity when $V \to V_0$. It then appears that the inequalities (A1) in fact only concern the boundary conditions at the wall and infinity. Plots of $\alpha_e(U_{e0}, V_a)$ and $\alpha_i(U_{i0}, V_0)$ for these two extreme cases are shown in figure 17.

For ions, (A1) is satisfied for any value of U_{i0} and then no condition on the initial velocity arises in this

$V_a \leq V_0$ case. The potential $V(x)$ decreases monotonically when approaching the wall surface, and so α_i increases. The first branch of Lambert functions, $W_0(\alpha)$, tends monotonically toward 0 for increasing argument, while the second branch, $W_{-1}(\alpha)$, tends towards infinity (Fig. 2). Then, if the ion square velocity U_i were to be represented by the W_0 branch, it would imply a deceleration of ions when approaching the wall surface. However, the ion velocity is expected to increase, and therefore the W_{-1} branch must apply for the ion solution for the case $V_a \leq V_0$, and so $U_{i0} \geq 1$.

Regarding electrons, the argument $\alpha_e(U_{e0}, V_a)$ always crosses the lower limit $-\frac{1}{e}$ at two points in Fig. 17, whose values for U_{e0} are also given by Lambert functions using (A1):

$$U_{e0}^{\max} = -W_0\left[-e^{\frac{2(V_a-V_0)}{T_e}-1}\right] \leq 1,$$
$$U_{e02} = -W_{-1}\left[-e^{\frac{2(V_a-V_0)}{T_e}-1}\right] \geq 1. \quad \text{(A2)}$$

For both points the electron square normalized velocity at the wall takes the value $U_e = 1$, i.e. $u_e = u_{\text{th}e}$ at the wall, since $\alpha_e = -\frac{1}{e}$ in (10). The solutions with $U_{e0} \geq U_{e02}$ correspond to initial velocities u_{e0} greater than $u_{\text{th}e}$ and would be described by the W_{-1} branch of the Lambert function. According to these solutions, the electrons would come from infinity with a "high" convective velocity and would be decelerated as they approach the wall. However, considering particle flux conservation, if the convective velocity of electrons was to decrease, their density should on the contrary increase when approaching the wall to maintain the constant flux. As we expect the opposite to occur, these solutions can be eliminated. On the other hand, solutions for $U_{e0} \leq U_{e0}^{\max} \leq 1$ correspond to initial velocities lower than $u_{\text{th}e}$ and are described by the W_0 branch, for which electrons are correctly predicted to be accelerated towards the wall. Then, in this $V_a < V_0$ case the solutions to (10) are given by (11) and (12).

Appendix B: 1D cylindrical solution

1. Around the ion sonic radius R_S:

A mathematical difficulty arises at the sonic radius regarding density and velocity gradients for the field accelerated species, because both numerator and denominator in the derivative of (30) and (37) vanish at $r = R_S$. This indeterminacy can be overcome by using a Taylor expansion for the electric potential around R_S and performing a power series expansion[29] of velocity and density expressions around R_S. As an example we show here the development for the $V_a \leq V_0$ case.

We define the net charge density at $r = R_S$ to be:

$$Q_S = q(n_i(R_S) - n_e(R_S))$$

$$= qn_0 \left[e^{-\frac{1}{2} - \frac{V_S - V_0}{T_i}} - e^{\frac{1}{2}W_0\left[-\frac{R_p^2}{R_S^2} e^{\frac{2(V_a - V_S)}{T_e}} - 1 \right] + \frac{V_S - V_0}{T_e}} \right] \quad (B1)$$

Then from (38) and (39) we get:

$$[\partial_r^2 V]_{R_S} = -\frac{Q_S}{\varepsilon_0} - \frac{T_i}{R_S^2}. \quad (B2)$$

According to (38) and (B2), a second order Taylor expansion of the potential around R_S can be expressed as:

$$V = V_S + \frac{T_i}{R_S}\epsilon - \frac{1}{2}\left(\frac{Q_S}{\varepsilon_0} + \frac{T_i}{R_S^2} \right)\epsilon^2, \quad (B3)$$

with $\epsilon = r - R_S$. Using (B3), the Taylor expansions of U_i and n_i around R_S can be expressed, from which the first derivatives at the sonic radius are identified to be:

$$[\partial_r U_i]_{R_S} = -\sqrt{\frac{2Q_S}{\varepsilon_0 T_i}},$$

$$[\partial_r n_i]_{R_S} = n_0 e^{-\frac{1}{2} + \frac{V_0 - V_S}{T_i}}\left(\sqrt{\frac{Q_S}{2\varepsilon_0 T_i}} - \frac{1}{R_S} \right). \quad (B4)$$

It then appears that the charge separation Q_S gives directly the gradient of the ion square velocity at the sonic radius. We also note from (B4) that the charge separation at R_S must be positive, $n_i(R_S) \geq n_e(R_S)$, for $[\partial_r U_i]_{R_S}$ and $[\partial_r n_i]_{R_S}$ to be real numbers, as expected for $V_a \leq V_0$. Furthermore, as in most cases we expect the ion density to increase with r, we can express from (B4) the condition:

$$[\partial_r n_i]_{R_S} \geq 0 \Rightarrow Q_S \geq \frac{2\varepsilon_0 T_i}{R_S^2}. \quad (B5)$$

The inequality (B5) defines an upper value for V_S but can unfortunately not be solved analytically.

In the $V_a \geq V_0$ case the density and velocity gradients for electrons at the sonic radius are given by:

$$[\partial_r U_e]_{R_S} = -\sqrt{\frac{-2Q_S}{\varepsilon_0 T_e}},$$

$$[\partial_r n_e]_{R_S} = n_0 e^{-\frac{1}{2} - \frac{V_0 - V_S}{T_e}}\left(\sqrt{\frac{-Q_S}{2\varepsilon_0 T_e}} - \frac{1}{R_S} \right). \quad (B6)$$

As expected the charge separation is now to be negative in order to obtain real quantities. The electron density is expected to increase with r, such as we can express from (B6) the following condition on the charge separation at the sonic radius in the $V_a \geq V_0$ case:

$$[\partial_r n_e]_{R_S} \geq 0 \Rightarrow Q_S \leq -\frac{2\varepsilon_0 T_e}{R_S^2}. \quad (B7)$$

Coming back to the general case, the range of possible values for V_S can be analytically limited by considering
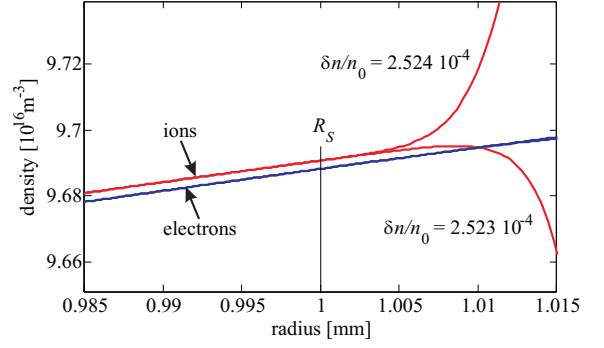

FIG. 18. Electron and ion densities around the ion sonic radius R_S obtained by integration of Poisson's equation for two close values of Q_S (0.04% variation). Fixed parameters: Argon gas, $n_0 = 10^{17}$ m^{-3}, $T_e = 3$ V, $T_i = 0.2$ V, $V_0 = 20$ V, $V_a = 15$ V, probe radius $R_p = 0.25$ mm.

first that the density of the field accelerated species at the sonic radius cannot exceed its initial density at infinity n_0, and secondly that the density of the field repelled species at the sonic radius must be smaller than that of the field accelerated one ($Q_S \geq 0$ for $V_a \leq V_0$ and $Q_S \leq 0$ for $V_a \geq V_0$).

Considering the case $V_a \leq V_0$ we get:

$$V_0 - \frac{T_i}{2} \leq V_S \leq V_0 - \frac{\Theta}{2} - \frac{T_i}{2}W_0[-\frac{\Theta R_p^2}{T_i R_s^2}e^{\frac{2(V_a - V_0)}{T_e} - \frac{\Theta}{T_i}}] \quad (B8)$$

where $\Theta = \frac{T_e T_i}{T_e + T_i}$.

For $V_a \geq V_0$ the range for V_S is given by:

$$V_0 + \frac{T_e}{2} \geq V_S \geq V_0 + \frac{\Theta}{2} + \frac{T_e}{2}W_0[-\frac{\Theta R_p^2}{T_e R_s^2}e^{\frac{-2(V_a - V_0)}{T_i} - \frac{\Theta}{T_e}}] \quad (B9)$$

2. Iterative integrations

For a given R_S the result of Poisson integration in the direction of increasing r is extremely sensitive to the value taken for Q_S (i.e. V_S through (B1)). This is illustrated for a $V_a \leq V_0$ case on figure 18 which represents the evolution of the electron and ion densities for two very close values of Q_S (0.04% variation). A too high charge separation at R_S (i.e. velocity and density gradients too steep (B4)) leads to an ion density which diverges toward $+\infty$, while, on the other hand, a too low charge separation leads to an ion density which diverges toward $-\infty$. The divergences occur especially when the space charge density Q becomes small, and are then so sensitive that one can try to adjust the value of Q_S up to many decimal places without really improving the obtained density profiles. Nevertheless, Q_S can then be iteratively determined by detecting this positive/negative divergence switching. Apart from this numerical determination, we would need a criterion on Q_S that would ensure $V(r \to \infty) = V_0$. Such a criterion cannot be deduced for the cylindrical
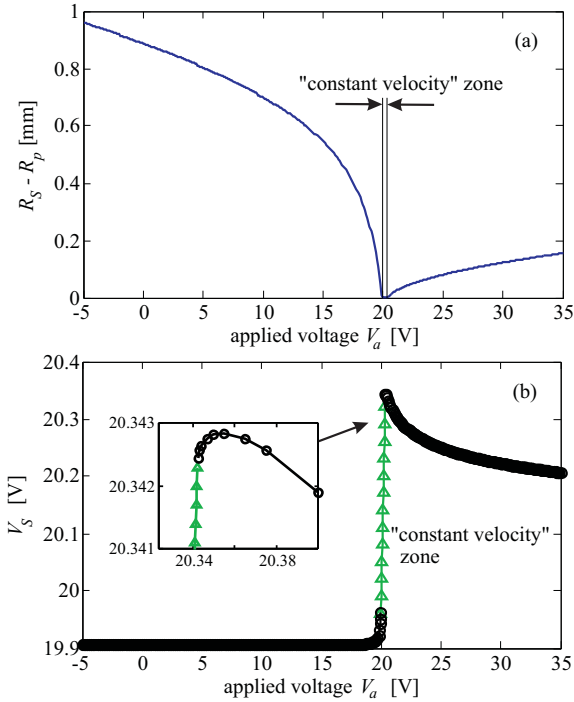
FIG. 19. (a) Evolution of the sonic radius R_S with probe bias potential V_a, for probe radius $R_p = 0.15$ mm. The "constant velocity" zone extends approximately between $V_{\lim} = 19.955$ V$< V_0$ and $V_{\lim} = 20.342$ V$> V_0$. (b) Evolution of the electric potential V_S at the sonic radius with V_a. The triangles represent the "constant velocity" zone solution $V_S(V_a) = V_a$, while the circles correspond to computed solutions outside of the "constant velocity" zone. The inset shows a zoom around the limit potential for $V_a \geq V_0$. Fixed parameters: Argon gas, $n_0 = 10^{17}$ m^{-3}, $T_i = 0.2$ V, $T_e = 3$ V, $V_0 = 20$ V.

case in the same way as for the 1D Cartesian case (using $[\partial_V |Q|]_{V_0} \leq 0$) because all the expressions vanish at infinity. Fortunately, the integration of Poisson's equation towards the probe (decreasing r) is not so sensitive to the value taken for Q_S, and only a few iterations are needed to estimate the voltage profile between R_S and R_p with a sufficient resolution (1% in Fig. 9).

3. Voltage dependence of the sonic radius parameters

The typical evolution ($R_p = 0.15$ mm) of the sonic radius R_S with the applied probe potential V_a is shown in Fig. 19(a). It can be seen that the "constant velocity" zone for which $R_S = R_p$, and both electron and ion velocities are taken to be constant ($u_s = u_{ths}$), is of small extent. It was found that the width of the "constant velocity" zone depends on the probe radius, lower R_p leading to wider zones. The increase of R_S with the applied potential was found to be the only reason for the non-saturation of the ion and electron currents. To illustrate this point we consider as an example the electron current non-saturation for $V_a > V_0$. In this case, the
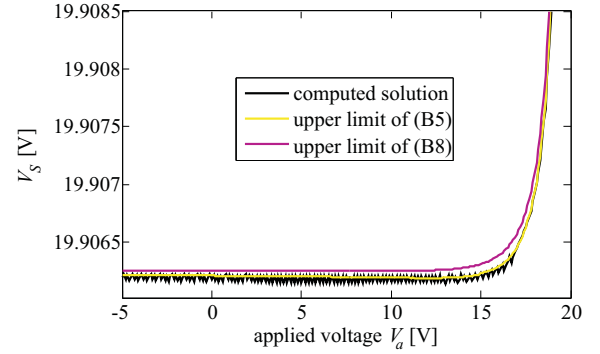

FIG. 20. Evolution of the electric potential V_S as a function of the applied probe potential $V_a \leq V_0$, for $R_p = 0.15$ mm. The noisy black curve corresponds to computed values. The yellow curve is the solution of (B5) while the red one corresponds to the analytical upper value for V_S according to (B8). Fixed parameters: Argon gas, $n_0 = 10^{17}$ m^{-3}, $T_i = 0.2$ V, $T_e = 3$ V, $V_0 = 20$ V.

ion contribution to the total current can be neglected, so that the electron flux to the probe $\Gamma_e = 2\pi R_S u_{the} n_{eS}$ determines the collected current. It can been verified (not shown) that n_{eS} decreases slightly (by a few percent) with increasing bias, and therefore the non-saturation of the electron flux can only be due to the increase in R_S with V_a. Similar reasoning can be applied for the non-saturation of ion current.

Figure 19(b) shows the evolution of the sonic radius potential V_S with the probe potential. We first note that the solution computed in the V_a ranges for which R_S can be defined seems to tend tangentially toward the "constant velocity" zone solution $V_S(V_a) = V_a$ at both limit potentials $V_{\lim}$. Fig. 20 shows a zoom on $V_S(V_a)$ for the $V_a \leq V_0$ range, along with the analytic upper limit for V_S given by (B8), which corresponds to a vanishing charge separation at the sonic radius. The computed upper limit given by (B5) expresses the condition for vanishing ion density gradient at R_S. The fact that the computed values of V_S deviate only slightly from these limit curves is a consequence of the very small charge separation at the sonic radius for $V_a \leq V_0$. This then cannot be generalized to the $V_a \geq V_0$ case for which it was shown that the charge separation at R_S is large.

4. Analysis of cylindrical probe characteristics

We describe here how the cylindrical solution given in this work can be used to analyse experimental IV characteristics in a simple way. To illustrate the method we consider as an example a theoretical characteristic $J_p(V_a)$ computed for $R_p = 0.15$ mm, taken from Fig. 10, as shown on Fig. 21(a).

First, radial probes characteristics are generally expected to present an inflexion point in the vicinity of
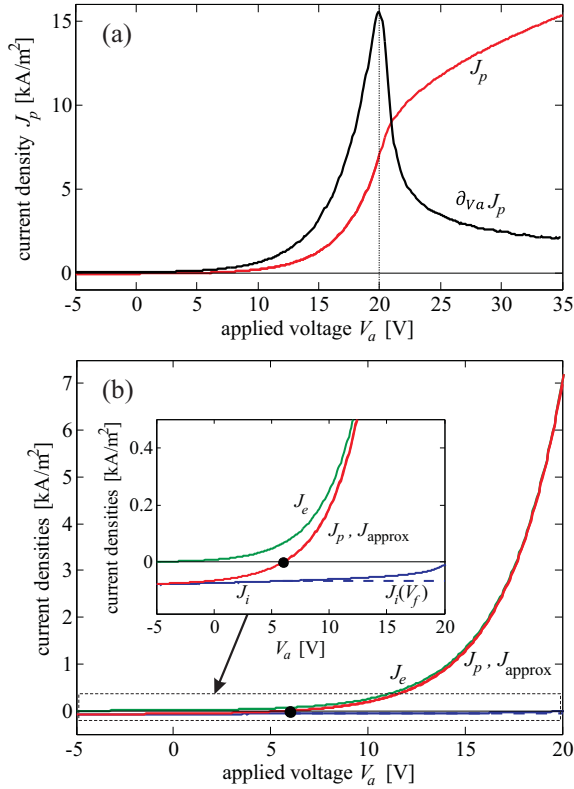
FIG. 21. (a) *IV* characteristic calculated for $R_p = 0.15$ mm, with the first derivative $\partial_{V_a} J_p(V_a)$, whose maximum indicates the plasma potential. (b) The probe current J_p and the approximated current J_{approx}, which are indistinguishable in these graphs, and the electron current J_e; the inset shows an expanded scale of the currents around the floating potential V_f (marked by a black dot at $J_p = 0$), along with the ion current J_i and the constant ion current $J_i(V_f)$ (dashed line). Fixed parameters: Argon gas, $n_0 = 10^{17}$ m^{-3}, $T_i = 0.2$ V, $T_e = 3$ V, $V_0 = 20$ V.

the plasma potential V_0. This is illustrated on Fig. 21(a) showing the first derivative $\partial_{V_a} J_p(V_a)$, which reaches its maximum slightly before $V_a = V_0$. Theoretically, for big radius probes this inflexion point is exactly at V_0. It is sometime difficult to determine precisely this point from real measurements, but it provides a fair order of magnitude. Another particular point of the characteristic is the floating potential V_f, for which ion and electron contributions to the total current are equal. We propose an analysis of the portion of the curve comprised between the floating potential and the plasma potential.

According to the model, electron and ion currents (J_e and J_i respectively) at the probe surface are given by:

$$J_e = q u_{\text{the}} n_0 e^{-\frac{1}{2}} e^{\frac{V_a - V_0}{T_e}}, \quad \text{(B10)}$$

$$J_i = -q u_{\text{thi}} n_0 \sqrt{U_i(V_a)} e^{-\frac{U_i(V_a)}{2} - \frac{V_a - V_0}{T_i}}. \quad \text{(B11)}$$

with

$$U_i = -W_{-1}\left[-\frac{R_S^2}{R_p^2} e^{\frac{-2(V_S - V_a)}{T_i} - 1} \right].$$

Plots of J_e and computed J_i in the range $V_a = [V_f, V_0]$ are shown on figure 21(b). The relation (B11) is quite unpractical to use because both evolutions of R_S and V_S with the applied bias V_a are unknown, and must be computed for a given probe radius R_p. But, as can be seen on the inset of figure 21(b), the ion contribution J_i to the total current $J_p = J_e + J_i$ is rapidly negligible with respect to the electron one. In fact, we would make only a small error by considering the ion contribution to be constant between V_f and V_0, this constant being given by the value of J_i at the floating potential. According to equation B10 we have:

$$J_i(V_f) = -J_e(V_f) = -q u_{\text{the}} n_0 e^{-\frac{1}{2}} e^{\frac{V_f - V_0}{T_e}},$$

therefore the total collected current $J(V_a)$ in the $[V_f, V_0]$ interval approximates to:

$$J_{\text{approx}}(V_a) = J_i(V_f) + J_e(V_a)$$
$$= q u_{\text{the}} n_0 e^{-\frac{1}{2} - \frac{V_0}{T_e}} \left[e^{\frac{V_a}{T_e}} - e^{\frac{V_f}{T_e}} \right]. \quad \text{(B12)}$$

We then obtain an expression which is independent of unknown parameters R_S and V_S, and on the probe radius R_p as well. The impact of R_p on the characteristic is in fact taken into account through the experimental determination of the floating potential V_f, which depends on the probe radius as can be seen in (40). The difference between the originally-computed characteristic $J_p(V_a)$ and the approximate expression $J_{\text{approx}}(V_a)$ is so small as to be practically indistinguishable on Figs. 21(a) and (b) for $V_a \leq V_0$.

[1] F. F. Chen, *Electric Probes* (in "Plasma Diagnostic Techniques", ed. R. H. Huddlestone and S. L. Leonard, Academic Press, New York, 1965) Chap. 4, pp. 113–200.
[2] H. M. Mott-Smith and I. Langmuir, Phys. Rev. **28**, 727 (1926).
[3] L. Tonks and I. Langmuir, Phys. Rev. **34**, 876 (1929).
[4] J. E. Allen, Plasma Sources Sci. Technol. **18**, 014004 (2009).
[5] D. Bohm, *The Characteristics of Electrical Discharges in Magnetic Fields*, edited by A. Guthrie and R. K. Wakerling (New York: McGraw-Hill, 1949) p. 77.
[6] A. Caruso and A. Cavaliere, Nuovo Cimento **26**, 1389 (1962).
[7] S. A. Self, Phys. Fl. **6**, 1762 (1963).
[8] S. H. Lam, Phys. Fl. **8**, 73 (1965).
[9] R. N. Franklin and J. R. Ockendon, J. Plasma Phys. **4**, 371 (1970).
[10] V. A. Godyak and N. Sternberg, IEEE Trans. Plasma Sci. **18**, 159 (1990).
[11] K.-U. Riemann, J. Phys. D: Appl. Phys. **24**, 493 (1991).
[12] K.-U. Riemann, J. Tech. Phys. **41**, 89 (2000).
[13] R. N. Franklin and J. Snell, Phys. Pl. **8**, 643 (2001).
[14] R. N. Franklin, J. Phys. D: Appl. Phys. **36**, R309 (2003).
[15] K.-U. Riemann, Plasma Sources Sci. Technol. **18**, 014006 (2009).
[16] K.-U. Riemann, Plasma Sources Sci. Technol. **18**, 014007 (2009).
[17] R. M. Crespo, Plasma Sources Sci. Technol. **24**, 045012 (2015).
[18] A. Din, Phys. Pl. **23**, 083505 (2016).
[19] D. Bohm, E. H. S. Burhop, and H. S. W. Massey, *The Characteristics of Electrical Discharges in Magnetic Fields*, edited by A. Guthrie and R. K. Wakerling (New York: McGraw-Hill, 1949) Chap. 2, p. 13.

[20] J. E. Allen, R. L. F. Boyd, and P. Reynolds, Proc. Phys. Soc. **70**, 297 (1957).

[21] I. B. Bernstein and I. N. Rabinowitz, Phys. Fl. **2**, 112 (1959).

[22] E. R. Harrison and W. B. Thompson, Proc. Phys. Soc. (London) **74**, 145 (1959).

[23] K.-B. Persson, Phys. Fl. **5**, 1625 (1962).

[24] P. D. Prewett and J. E. Allen, J. Plasma Phys. **10**, 451 (1973).

[25] G. A. Emmert, R. M. Wieland, A. T. Mense, and J. N. Davidson, Phys. Fl. **23**, 803 (1980).

[26] F. F. Chen, J. D. Evans, and D. Arnush, Phys. Pl. **9**, 1449 (2002).

[27] I. H. Hutchinson, *Principles of Plasma Diagnostics* (Cambridge University Press, 2nd ed., 2002).

[28] M. A. Lieberman and A. J. Lichtenberg, *Principles of Plasma Discharges and Materials Processing* (John Wiley and Sons, 2nd ed., Hoboken, New Jersey, 2005).

[29] R. M. Corless, G. H. Gonnet, D. E. G. Hare, D. J. Jeffrey, and D. E. Knuth, Adv. Comput. Math. **5**, 329 (1996).

[30] B. A. Alterkop, I. D. Dubinova, and A. E. Dubinov, J. Exp. Theor. Phys. **102**, 173 (2006).

[31] B. Scheiner, S. D. Baalrud, B. T. Yee, M. M. Hopkins, and E. V. Barnat, Phys. Pl. **22**, 123520 (2015).

[32] J. G. Laframboise, *Univ. of Toronto, Institute for Aerospace Studies, UTIAS Report No. 100* (unpublished, 1966).

[33] R. N. Franklin and J. Snell, Phys. Pl. **7**, 3077 (2000).

[34] V. Pletnev and J. G. Laframboise, Phys. Pl. **13**, 073503 (2006).

[35] V. N. Duarte and R. A. Clemente, Phys. Pl. **18**, 043504 (2011).

[36] M. J. M. Parrot, L. R. O. Storey, L. W. Parker, and J. G. Laframboise, Phys. Fl. **25**, 2388 (1982).

[37] P. Cagas, A. Hakim, J. Juno, and B. Srinivasan, Phys. Pl. **24**, 022118 (2017).

[38] J. Loizu, P. Ricci, and C. Theiler, Phys. Rev. E **83**, 016406 (2011).

[39] S. D. Baalrud and C. C. Hegna, Plasma Sources Sci. Technol. **20**, 025013 (2011).

[40] S. D. Baalrud, J. D. Callen, and C. C. Hegna, Phys. Rev. Lett. **102**, 245005 (2009).

[41] N. Sternberg and V. Godyak, IEEE Trans. Plasma Sci. **35**, 1341 (2007).

[42] L. C. Woods, *An Introduction to the Kinetic Theory of Gases and Magnetoplasmas* (Oxford University Press Inc., New York, 1993) p. 46.

[43] F. F. Chen and D. Arnush, Phys. Pl. **8**, 5051 (2001).

[44] N. Hershkowitz, Phys. Pl. **12**, 055502 (2005).

[45] K.-U. Riemann, IEEE Trans. Pl. Sci. **23**, 709 (1995).

[46] S. D. Baalrud, B. Scheiner, B. Yee, M. Hopkins, and E. Barnat, Plama Phys. Control. Fusion **57**, 044003 (2015).

[47] P. M. Chung, L. Talbot, and K. J. Touryan, *Electric Probes in Stationary and Flowing Plasmas: Theory and Application* (Springer-Verlag, New York, 1975).

[48] F. F. Chen, J. Appl. Phys. **36**, 675 (1965).

[49] F. F. Chen, Plasma Sources Sci. Technol. **18**, 035012 (2009).

[50] F. F. Chen, Phys. Pl. **8**, 3029 (2001).

(a)

wall | V_a | collisionless plasma | $\leftarrow$ u_{i0} particle flux source, density n_0 potential V_0

$\leftarrow$ u_{e0}

0 | x

(b)

probe | V_a | 0 | R_p | collisionless plasma | $\leftarrow$ $u_{i0}=0$ eq^{bm} plasma, density n_0 potential V_0

$\leftarrow$ $u_{e0}=0$

r

(c)

big probe | V_a | sheath edge, density n_{sh} potential V_{sh} | eq^{bm} plasma, density n_0 potential V_0

collisionless sheath | $\leftarrow$ u_{ish} | quasi-neutral pre-sheath | $\leftarrow$ $u_{i0}=0$

$\leftarrow$ u_{esh} | $\leftarrow$ $u_{e0}=0$

(a) infinite plane wall, $V_a < V_0$

- potential [V]: $V_0 = 20$ V, $V_a = 15$ V
- density [10^{16} m^{-3}]: n_i, n_e, n_0
- norm. velocity, u/u_{th}: $u_i / u_{\text{th}i}$, $u_{\text{Bohm}} / u_{\text{th}i}$, $u_e / u_{\text{th}e} = 1$, $u_e / u_{\text{th}e}$
- distance from wall [mm]

(b) $V_a > V_0$

- potential [V]: $V_a = 25$ V, $V_0 = 20$ V
- density [10^{16} m^{-3}]: n_e, n_i, n_0
- norm. velocity, u/u_{th}: $u_e / u_{\text{th}e}$, $u_i / u_{\text{th}i} = 1$, $u_i / u_{\text{th}i}$
- distance from wall [mm]

cylindrical probes
(a) $V_a < V_0$

$V_0 = 20$V

$V_a = 15$V

n_i

n_e

u_i / u_{thi}

R_S

R_S

R_S

u_e / u_{the}

(b) $V_a > V_0$

$V_a = 25$V

$V_0 = 20$V

n_e

n_i

u_e / u_{the}

R_S

R_S

R_S

u_i / u_{thi}

radius from probe axis, r [mm]

(a) current density J_p [kA/m²] vs applied voltage V_a [V]

big radius probe

classical probe

(b) ion & electron currents [A/m²] vs applied voltage V_a [V]

J_e^{big}

$J_i^{\text{classical}}$

$J_e^{\text{classical}}$

J_i^{big}

(c) current density J_p [A/m²] vs applied voltage V_a [V]

V_f

big radius

classical

probe

vessel wall

$\phi_s = 0$

ϕ_s to the probe

ϕ_s to the vessel wall

r_0

$r = 0$

r

(a)

J_p

$\partial_{Va} J_p$

current density J_p [kA/m^2]

applied voltage V_a [V]

(b)

J_e

J_p , J_{approx}

J_i

$J_i(V_f)$

current densities [kA/m^2]

V_a [V]

J_e

J_p , J_{approx}

current densities [kA/m^2]

applied voltage V_a [V]